TOWARDS A HIGH QUALITY POLARIZATION-ENTANGLED MULTI-PHOTON SOURCE

POH HOU SHUN

(B.Sc. (Hons.)), NUS

A THESIS SUBMITTED FOR THE DEGREE OF MASTER OF SCIENCE

DEPARTMENT OF PHYSICS
NATIONAL UNIVERSITY OF SINGAPORE

2009

Acknowledgements

No journey of scientific discovery is ever truly taken alone. Every step along the way, we encounter people who are a great source of encouragement, guidance, inspiration, joy, and support to us. The journey I have embarked upon during the course of this project is no exception.

Firstly, I would like to extend my heartfelt thanks and gratitude to Lum Chune Yang, Ivan Marcikic, Lim Jiaqing, and Ng Tien Tjeun, exceptional researchers whom I have the pleasure of working with on various experiments over the years. They have endured with me through endless late night in the lab, going down numerous dead ends before finally getting the experiments up and running.

Special thanks also to my two project advisors, Antía Lamas-Linares and Christian Kurtsiefer for their constant guidance on and off the project over the years. Despite their hectic schedule, they still took great pains to go through the draft for this thesis, making sure is up to scratch for submission.

A big and resounding thanks also goes out to my other fellow researchers and colleagues in CQT, Alexander Ling, Brenda Chng, Caleb Ho, Chin Pei Pei, Darwin Gosal, Gan Eng Swee, Gleb Maslennikov, Ilja Gerhardt, Matthew Peloso, Syed Abdullah Aljunied, and Tey Meng Khoon. They are a source of great inspiration, support, and joy during my time in the group.

Finally, I would like to thank my friends and family for their kind and constant words of encouragement. They always remind me of the truly important things in life whenever I find myself slightly off course on this journey of discovery.

Contents

Summary

This thesis documents my research on the setting up, characterization, and optimization of a polarization-entangled multi-photon source. The photon pairs are produced by spontaneous parametric down-conversion (SPDC) process pumped by ultrafast optical pulses. I will focus on the characterization of how spectral distinguishability between the down-conversion paths leads to a degraded polarization entanglement quality, commonly observed in such a configuration, and the implementation of a spectral compensation scheme to eliminate the distinguishability. The goal of this research is to produce a source of polarization-entangled multi-photon state with high brightness and fidelity which can be used for various quantum communication protocols and fundamental tests of quantum physics in higher-dimensional Hilbert spaces.

SPDC is the most common process by which entangled photons are generated. The initial experiments on SPDC and applications for quantum key distribution make use of pump light from continuous-wave (cw) lasers, where entangled states can be prepared efficiently with high fidelity in various degrees of freedom.

The other regime covers experiments in which photon pairs need to exhibit tight localization in time, or when more than one pair should be generated simultaneously. In such cases, short optical pulses with a coherence time compatible with that of the down-converted photons have to be used as a pump. From existing theoretical studies it is known that the combination of the broadband pump with the dispersion relations of the nonlinear optical material leads to entanglement of the polarization degree of freedom with the spectral properties of the down-converted photons. When only the polarization degree of freedom is considered, this results in a degree of mixedness, leading to a degraded entanglement quality. Typically, strong spectral filtering is applied in order to detect only photons which fall into the non-distinguishable part of the spectrum. In the first half of the thesis, I will present an experimental investigation of the phenomenon mainly through the joint spectral mapping of the polarization correlations in each decay path.

In multi-photon experiments where the coincidence rate decreases rapidly with any filter loss, spectral filtering can be extremely disadvantageous. The spectral compensation scheme proposed and first implemented by Kim *et al.* [1] can eliminate the spectral distinguishability without significant loss of signal and thus benefits these experiments greatly. In the second half of the thesis, I will give a detailed account of the implementation of this spectral compensation scheme. Characterization of the source after spectral compensation showed that the spectral distinguishability between the decay paths could be eliminated.

For certain systems it is possible to determine the presence of entanglement by appealing to an entanglement witness like the Clauser-Horne-Shimony-Holt (CHSH) inequality. In the last part of the thesis, I will present results from such a measurement carried out using the earlier experimental setup. I will then conclude with some remarks on the remaining issue known to be restricting the entanglement quality of the higher-order states and implementation with which it can be resolved.

List of Figures

List of Tables

Chapter 1

From Quantum Mechanics to Quantum Information and Computation

We now live in an era of information. Almost all the activities going on daily, ranging from the simple bank transaction to the way scientific research is conducted, rely on information. Transparent to most of us, information also supports the security and communication that underlies these activities. Often, computers of one form or another retrieve, communicate, process, and store this information.

This is a far cry from the very first fully programmable electronic computer, the Electronic Numerical Integrator And Computer or ENIAC, built by the University of Pennsylvania for the United States Army during World War II to analyze the trajectory of artillery rounds. ENIAC had more than 10000 vacuum tubes which occupied a large room and required a number of staffs to operate and maintain.

All these changed with the arrival of the first quantum revolution which brought us the transistor. The first solid state transistor, invented at Bell Laboratories on December 16, 1947 by William Shockley, John Bardeen, and Walter Brattain, began as a study into the flow of electrons over the surface of a semiconductor. The smaller and more energy efficient transistor ultimately replaced the vacuum tube. Since then, increasing level of miniaturization enabled more transistors to be fitted onto a single

silicon chip, resulting in more powerful and energy efficient processors for computers. However, despite all the technological advances, the majority of quantum phenomenon remains untapped as resources for communication and computation. Both the bits of information and the physical systems on which they are encoded are essentially classical in nature.

Following the significant progress made in the field of experimental Physics over the past two decades, we are becoming increasingly proficient in the fabrication and manipulation of physical systems which demonstrate quantum effects. With this next quantum revolution, we see experiments starting to use the various degrees of freedom available in a number of quantum systems to encode quantum bits of information or qubits. Some of these first experiments [2, 4] used the polarization degree of a photon to encode the qubit. These photonic qubits have the advantage of easy generation and are relatively resistant to decoherence. Thus they remain widely used in various experiments [6, 7, 8, 9, 10] till today.

The qubit exhibits the features of non-cloneability, superposition, and can be entangled in multi-qubit states, all of which are purely quantum mechanical effects. When photonic qubits are entangled in a multi-photon state, they can be used for various quantum communication protocols [11, 12] and fundamental tests of quantum physics in higher-dimensional Hilbert spaces [13, 14, 15]. Multi-photon states also allow certain classes of computational tasks [16, 17] which are either inefficient or impractical on classical information processing system to be carried out. This thesis focuses on the experimental aspects of the generation of these multi-photon states for quantum communication and computation.

1.1 Qubit, The Quantum Mechanical Bit

The classical bit is the most fundamental unit of digital information. It is a representation of a binary digit, taking a logical value of either "1" or "0". Due to the binary nature of the bit, digital information can be encoded in any physical system which has two stable states such as the direction of magnetic domain on a magnetic media, the pits and bumps on the reflective layer on an optical disk or voltage levels in a digital circuit.

Over the past decades, we have seen experiments that allow us to study and manipu-

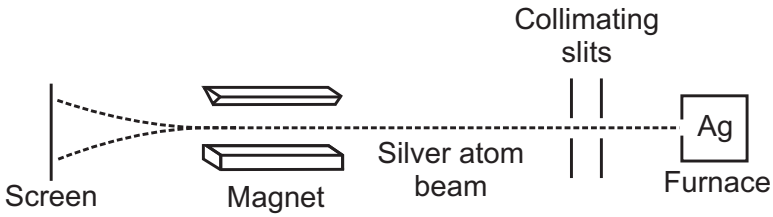

Figure 1.1: Stern-Gerlach experiment. A beam of neutral silver atom is collimated and directed through an inhomogeneous magnetic field. After passing through the inhomogeneous magnetic field, the beam splits into two. Since the silver atoms in the beam are neutral, any deflection of the silver beam can only be attributed to the intrinsic angular momentum of the unpaired electron in the silver atoms. Thus this experiment shows that the spin angular momentum of an electron along the direction defined by the magnetic field can only take one of two possible value, $+\frac{\hbar}{2}$ (spin-up) or $-\frac{\hbar}{2}$ (spin-down).

late physical systems which exhibit quantum behaviors being devised and implemented. In this quantum regime, the bit can be encoded in state of a spin-$\frac{1}{2}$ (two-level) system. The reason why a spin-$\frac{1}{2}$ system is also called a two-level system stemmed from an experiment performed by Otto Stern and Walther Gerlach in 1922 to study the intrinsic angular momentum of an electron. In what later came to be known as the Stern-Gerlach experiment (Fig. 1.1), they showed that the spin angular momentum of an electron along any direction can only take one of two possible value, $+\frac{\hbar}{2}$ (spin-up) or $-\frac{\hbar}{2}$ (spin-down). In the quantum state vector representation, spin-up and spin down can be written as $|\uparrow\rangle$ and $|\downarrow\rangle$, respectively. It is possible to manipulate the direction of the electron spins and by associating "1" to $|\uparrow\rangle$ and "0" to $|\downarrow\rangle$, this degree of freedom can be used essentially to encode qubits.

Apart from the spin of an electron, degrees of freedom of other quantum systems can also be used to encode the qubit. A few examples are the magnetic flux, charge or phase of superconducting circuits [18] and the energy levels [19] or nuclear spins [20] in atoms. By far the most commonly used physical carrier of the qubit in experiments is the photon. The photon has a number of degrees of freedom that can be used to encode a qubit: the number of photons in a specific mode (photon number) [21], arrival times of photons in an interferometric-type setup [22, 23], or the polarization [7, 24, 25]. Out of the three, the polarization of a photon is most often used to encode a qubit as they

are easy to generate, manipulate, and relatively resistance to decoherence.

These qubits exhibits the feature of non-cloneability, superposition, and can be entangled in multi-qubit states. All these characteristics are purely quantum mechanical in nature and they form the backbone for quantum information and quantum computation.

1.1.1 Non-cloneability

It is easy to copy a file on the computer. The copy of the file is in essence a prefect clone of the original. However, in quantum mechanics this is not generally true. This phenomenon is outlined in the non-cloning theorem [26, 27]. The theorem forbids the creation of identical copies of an arbitrary unknown quantum state. If a quantum cloning device is able to clone a state $|\psi\rangle$ with prefect fidelity, it is at most only able to do the same for the orthogonal state $|\psi\rangle^{\perp}$. For the special case of a spin-$\frac{1}{2}$ system, even under optimal condition, the maximum fidelity of cloning of an arbitrary unknown quantum state is shown only to be $\frac{5}{6}$ [28].

The no-cloning theorem has significant implications especially for the field of quantum key distribution (QKD). It prevents an eavesdropper from making perfect multiple copies of the qubits being distributed in the quantum channel, which in principle could be used, in conjunction with other resources, to gain full knowledge of the distributed key.

1.1.2 Superposition

A classical bit of information can take the logical value of either "0" or "1", but not both simultaneously. However, in the quantum regime, it is possible to prepare a quantum system such that it is in a state $c_0|0\rangle + c_1|1\rangle$, where c_0 and c_1 are the probability amplitudes and are in general both complex numbers. When we measure this qubit in the $|0\rangle$ and $|1\rangle$ basis state, the probability of the outcome is $|c_0|^2$ and $|c_1|^2$, respectively. As the absolute squares of the amplitudes equate to probabilities, it follows that c_0 and c_0 must be constrained by the equation $|c_0|^2 + |c_1|^2 = 1$, which means one will measure either one of the states. Such a two-level quantum system is said to be in a linear superposition of the $|0\rangle$ and $|1\rangle$ basis state and does not exist definitely in either states.

The advantage of superposition of states really comes in when we start dealing with system containing several qubits. Such a collection of N qubits is a called a quantum register of size N and can hold 2^N numbers. This is in contrast with a classical register of the same size which can only hold a single number. For example in the case of a two-qubit system register, a state consisting of superposition of the four combination is possible. The state of such a two-qubit system can be written as

$$|\Psi\rangle = c_{00}|00\rangle + c_{01}|01\rangle + c_{10}|10\rangle + c_{11}|11\rangle, \tag{1.1}$$

where c_{ij} is the probability amplitude of $|ij\rangle$. The notation $|ij\rangle$ means that qubit 1 and 2 are in state i and j, respectively.

Quantum algorithms make full use of this fact by being able to accept all the possible inputs pertaining to a certain computation task as linear superposition of basis states like in Eq. 1.1 and evaluate them in parallel. The required output from the evaluation is then obtained by suitable measurements done on the resulting state. It is this parallelism that gives quantum systems the edge over their classical counterparts in certain computational tasks. A brief discussion on what are the classes of computation problems that benefit from quantum parallelism is available in [29].

1.1.3 Entanglement

Quantum entanglement is a peculiar feature that is observed in some composite quantum systems. Essentially, the quantum mechanical state of certain systems consisting of two or more entities can no longer be adequately described by considering each of the component entity in isolation. A full description of such a composite quantum system is only possible by considering the system as a whole. This results in a kind of connection between the components that is quantum mechanical in nature and cannot be explained by classical correlations alone. These non-classical connections between entangled qubits are the essential requirements for the various quantum computation and communication protocols.

The very idea of quantum entanglement originated from a paper published by Albert Einstein, Boris Podolsky, and Nathan Rosen in 1935 [30] about their discussion on the completeness of the quantum mechanical description of reality. In their discussion, they considered a two-particle system (Fig. 1.2) prepared in a state with a well-defined relative position $x_1 - x_2$ and total momentum $p_1 + p_2$ at time $t = 0$. The particles

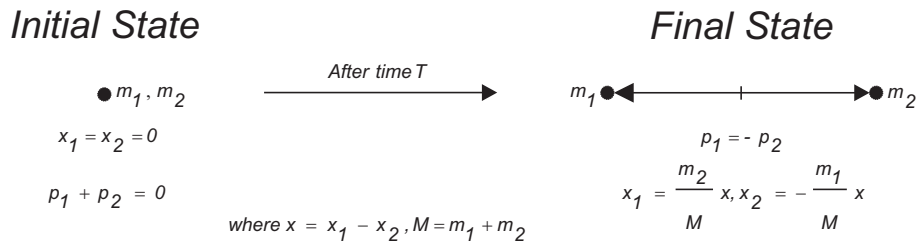

Figure 1.2: The EPR thought experiment. A two-particle system is prepared in a state with a well-defined relative position $x_1 - x_2$ and total momentum $p_1 + p_2$ at time $t = 0$. The particles are then permitted to interact from time $t = 0$ to $t = T$. After a certain amount of time $t > T$ when the particles are sufficiently separated such that they are no longer interacting, the position particle 1 is measured. From the measurement result, it is possible to assign a definite value to the position of particle 2 without changing the state. The same case can be repeated for the measurement of momentum. This contradiction with quantum mechanics came to be known as the EPR paradox.

are then permitted to interact from time $t = 0$ to $t = T$. After a certain amount of time $t > T$ when the particles are sufficiently separated such that they are no longer interacting, the position of particle 1 is measured. From the measurement result, it is possible to assign a definite value to the position of particle 2. The same case can be repeated for the measurement of momentum.

As the measurement of position or momentum of particle 1 will yield definite values for both particles, these quantities are, according to their definition, elements of reality. Since the two particles no longer interact with each other, the state of particle 2 is left unchanged by the measurement done on particle 1. This goes against quantum mechanics where the two operators of position and momentum do not commute. Measurement of the position of a particle will inadvertently change the state of the particle in such a way that it destroys all knowledge of the momentum, vice versa. This contradiction, which came to be known as the EPR paradox, forced them to conclude that the quantum mechanical description of physical reality given by wave functions is not complete.

For a complete description, they hypothesized that there are variables that correspond to all the elements of reality, giving rise to phenomenon of non-commuting

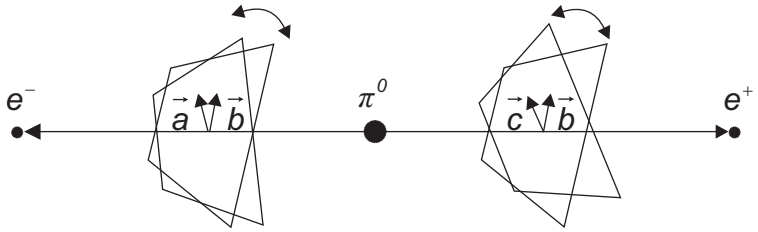

Figure 1.3: The EPR-Bohm thought experiment. An alternative version of the EPR experiment proposed by David Bohm in 1951. In the experiment, the decay of a neutral π meson act as a source of electrons and positrons which are entangled in their spins. Spin measurement of either the electron or positron in any arbitrary direction $\vec{a}$, $\vec{b}$, or $\vec{c}$ will have equal probability of yielding spin-up and spin-down. However, when comparing the results of the spin of both particle measured in the same direction, they show perfect anti-correlation.

quantum observables and the seemingly nonlocal effect that the measurement on one particle has on the state of the other. Such a theory is called local hidden variables (LHV) theory. It is only until later in the same year that Erwin Schrödinger used the term 'entanglement' to describe this kind of non-classical connection between the particles (an English translation of the original 1935 paper in German can be found in [31]).

In 1951 David Bohm came up with an alternative version of the EPR thought experiment [32] based on electron spins. This came to be known as the EPR-Bohm (EPRB) experiment. In the thought experiment (Fig. 5.1), he considered a source of electron and positron from the decay of a neutral π meson:

$$\pi^0 \rightarrow e^- + e^+. \tag{1.2}$$

As the pion has zero spin, by conservation of angular momentum, the electron and positron are in a singlet configuration described by

$$|\Psi^-\rangle = \frac{1}{\sqrt{2}}\left(|\uparrow_{e^-}\downarrow_{e^+}\rangle - |\downarrow_{e^-}\uparrow_{e^+}\rangle\right). \tag{1.3}$$

Spin measurement of either the electron or positron in any arbitrary direction $\vec{a}$, $\vec{b}$, or $\vec{c}$ will have equal probability of yielding spin-up and spin-down. However, when comparing the results of the spin of both particles measured in the same direction, they

show perfect anti-correlation. Such a two-particle system is said to be in an entangled state. The state of such a system as described by Eq. 5.2 can no longer be factorized into product of the two individual state.

Based on the Bohm experiment, John S. Bell came up with the Bell inequality [33] in 1987 which allows the prediction of quantum mechanics and LHV theories to be distinguished. It is derived based on arguments about measurement probabilities that result from classical correlations alone and imposes an upper limit for it. Quantum mechanics which can lead to stronger correlations will violate this limit. The original form of the Bell inequality is written as

$$|P(\vec{a},\vec{b}) \; - \; P(\vec{a},\vec{c})| \leq 1 \; + \; P(\vec{b},\vec{c}), \tag{1.4}$$

where $\vec{a}$, $\vec{b}$, and $\vec{c}$ are the direction of the spin measurements shown in Fig. 5.1. $P(\vec{a},\vec{b})$ is the average value product of the spins measured in direction $\vec{a}$ and $\vec{b}$, respectively. The measurement results will violate the Bell inequality only for certain systems when there is quantum entanglement between the particles.

In 1969 John F. Clauser, Micheal A. Horne, Abner Shimony, and Richard A. Holt rederived Bell inequality in a form that is no longer restricted to experiments where the measurement results only have two possible outcomes. This inequality later came to be known as the CHSH inequality [34]. It includes an experimentally determinable parameter S which is defined by

$$S \; = \; E(\theta_1,\theta_2) - E(\theta_1,\theta_2') + E(\theta_1',\theta_2) \; + \; E(\theta_1',\theta_2'). \tag{1.5}$$

The correlation function $E(\theta_1,\theta_2)$ for measurements with only two possible outcomes as in the case of Fig. 5.1 is given by

$$E(\theta_1,\theta_2) \; = \; P(\uparrow\uparrow \,|\theta_1,\theta_2) \; + \; P(\downarrow\downarrow \,|\theta_1,\theta_2) \; - \; P(\uparrow\downarrow \,|\theta_1,\theta_2) \; - \; P(\downarrow\uparrow \,|\theta_1,\theta_2), \tag{1.6}$$

where $P(\uparrow\uparrow \,|\theta_1,\theta_2)$ is the probability of obtaining spin-up for both particles with detectors orientated at angle θ_1 and θ_2, respectively.

For classical correlation, the parameter S will take values $|S| \leq 2$. The stronger quantum correlation will result in the violation of this inequality. Thus the parameter S can be used to quantify whether there is entanglement in a system above the limit expected from classical correlations alone.

It should be noted that due to the model on which the CHSH inequality is based, it is only applicable to bipartite systems containing even numbers of particles, i.e the particles are distributed evenly between two modes. A description of a special case of a Bell inequality for three particles can be found in [35]. However, the CHSH inequality can be extended to system with a larger even number of particles. Such systems are equivalent to the two-particle system but with more than two measurement outcomes. I will revisit this in more detail when I present an experiment to violate the spin-1 (three-level system) CHSH inequality in Chapter 5.

In the early 1980s Alain Aspect *et al.* conducted a series of experiments [2, 36, 37] aimed at violating the Bell inequality. In their experimental setup (Fig. 1.4), the polarization-entangled photons are generated via radiative atomic cascade of calcium. The photons then pass through polarizer (Pol), consisting of glass plates stacked at Brewster angle, which are detected by photomultiplier tubes (PM). A combination of a time-to-amplitude converter (T.A.C.) and a coincidence circuit detect photons arriving with 19 ns of each other. With the setup, they observed a violation of the Bell inequality by up to 9 standard deviations.

From that point on, there have been numerous realizations of the Bohm-type experiment using various entangled quantum systems. Currently, the polarization degree of freedom of the photon is by far the most commonly used physical property to encode the qubit. In the Aspect experiments, these polarization-entangled photons are generated by the atomic cascade of calcium. This has been replaced by the process of spontaneous parametric down-conversion (SPDC) in non-linear optical media for the generation of entangled photons in modern experiments. For the first part of Chapter 2. I will touch briefly on the theory of SPDC and what are some of the ways where the process can be used to generate entangled photons in experiments. In the second part of Chapter 2, I will describe in detail, a photon pair source using traditional type-II phase matching in a crossed-ring configuration [7] and its characterization.

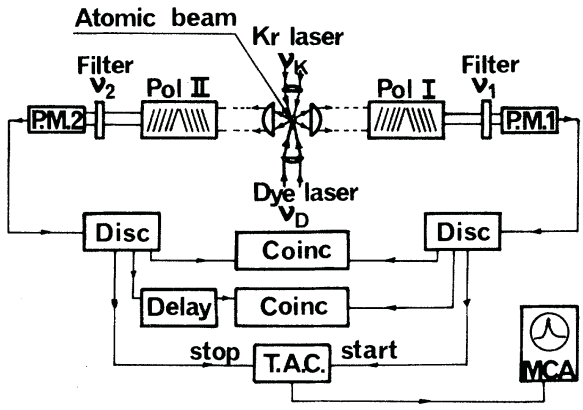

Figure 1.4: The experimental setup used by Alain Aspect *et al.* in the early 1980s to violate the Bell inequality. The polarization-entangled photons are generated via radiative atomic cascade of calcium. The photons then pass through polarizer (Pol), consisting of glass plates stacked at Brewster angle, to be detected by photomultiplier tubes (PM). A combination of a time-to-amplitude converter (T.A.C.) and a coincidence circuit detect photons arriving with 19 ns of each other. With the setup, they observed a violation of the Bell inequality by up to 9 standard deviations. (Figure adapted from [2])

1.2 Qubits in Applications of Quantum Information and Computation

The three quantum mechanical behaviors of non-cloneability, superposition, and entanglement exhibited by qubits form the basis of what makes their applications in quantum information and quantum computation possible. For the rest of this section, I will be presenting some of these applications with emphasis on systems utilizing photonic qubits.

1.2.1 Quantum Key Distribution

Some of the first theoretical proposals involving the use of photonic qubits that see implementation are in the field of quantum key distribution (QKD). There are a number of QKD protocols available* [38, 39, 40, 41, 42] of which two of them [38, 39] can be considered as milestones in the development of this field. The first of such protocols is proposed by Charles H. Bennett and Gilles Brassard in 1984 [38]. It later came to be known simply as BB84. BB84 uses the polarization of single photons to distribute keys unidirectionally from one party to another securely. It relies on the fact that any attempt to eavesdrop on the quantum channel by measuring the polarization states of the distributed photons will introduce detectable errors in the final key. No-cloning theorem prevents the eavesdropper from ever making prefect multiple copies of the distributed photons which he can use in principle to determine the polarization state of the photons without being detected. Due to the lack of a truly single photon source, BB84 has up till now been implemented with weak coherent pulses in various experiments [6, 43] and even in commercial QKD devices.†

While BB84 uses single photons to distribute keys, the protocol proposed by Artur K. Ekert in 1991 [39] makes use of polarization-entangled photons pairs. In this protocol, which came to be known as E91, polarization-entangled photons from a pair source is shared by two parties to distribute keys. Any attempt by the eavesdropper to measure the polarization state of the distributed photon will result in the disentangling of the two photons. To ensure that this is not the case, a Bell inequality measurement

*The five QKD protocols given here are BB84, E91, DPS, SARG04, and COW, respectively.

†Currently there are two companies, idQuantique and MagiQ Technologies, offering commercial QKD devices.

is conducted in parallel with the key distribution as a test of how secure is the quantum channel. This protocol, if operating in the device-independent scenario [44], in principle allows two parties distributing the key to use any pair source that violates the Bell inequality even though they may not be in control of the entangled source itself. In BB84 one party encodes the key in the polarization state of photons and distributed them to the other party. This is different from entanglement-based protocols like E91 where the entangled polarization state of the photon pair consists of a balanced linear supposition of two polarization combinations. Measurement by either parties will yield a random result of "1" or "0" thus giving rise to a truly random key. An experimental implementation of the protocol can be found in [45].

1.2.2 Quantum Algorithms

Quantum algorithms are designed to exploit the parallelism made possible by the linear superposition of basis qubit states to speed up certain computation tasks over classical computers. The first of such algorithms is proposed by David E. Deutsch in 1985 [46]. The Deutsch algorithm evaluates a binary function $f(x)$ that act on a one bit binary number. The function $f(x)$ is considered constant if $f(0) = f(1)$ and balanced if $f(0) \neq f(1)$. On a classical computer, it will take a minimum of two evaluations of the function $f(x)$ in order to obtain $f(0)$ and $f(1)$. However, on a quantum computer running Deutsch algorithm, it will only take one such evaluation. This is due to the fact that for quantum algorithms such as the Deutsch algorithm, it is possible to input a linear superposition of basis qubit states like Eq. 1.1. All these input combinations get evaluated in parallel and suitable measurements at the end of the evaluation are made to obtain the result. A general version of the Deutsch algorithm for an N-bit function is found in [47].

The next quantum algorithm, proposed by Peter Shor in 1994 [16], sparked off huge interest in the field due to the serious implication it has on the security of commercial and private communications. One of the strongest classical encryption scheme available is the RSA encryption [48]. It is based on the fact that the factorization of the product of two large prime numbers is much more computationally intensive than the product of the two prime numbers themselves. Classical computers will take on average $N2^N$ operations to decipher a key of N bits. Even a modest key of $N = 128$ bit long is well

beyond the capability of current computer technology to decipher. By contrast a quantum computer running Shor's algorithm will only take on average N^2 operations [49]. It should be noted that the number of bits quantum computers need to operate on in order to be useful is still considerably larger than anything that is currently experimentally feasible. The latest experimental efforts manage to demonstrate the factor of 15 are 3 and 5 with four photonic qubits [50, 51].

Another prominent quantum algorithm is proposed by Lov K. Grover in 1996 [17]. The Grover's algorithm is often termed as a quantum search algorithm. However, a more accurate description of the function of the algorithm is as an inverting algorithm. The algorithm have the functionality of a search algorithm as the inversion of the probability amplitude only happens for basis state with the matching search criterion. Typically on a classical computer it will take on average $\frac{N}{2}$ steps to search through a database with N entries. Grover's algorithm improves that by requiring only on average $\sqrt{N}$ operations [49] to search though the same database. The algorithm works on the fact that the unitary operator that does the inversion operate on all the basis states in the linear superposition. Successive call of the Grover algorithm increases the probability that the system is in the solution state. When the probability is within tolerance, the iteration is stopped. There have been a number of experimental realization of the algorithm with qubit pairs [52, 53].

1.2.3 Quantum Computation and Quantum Communication

In classical computing, no matter how complex an information processing operation is, it can be broken down into the action of a specific combination of simple binary logic gates such as the NOT or NAND gates. These gates operate either on one or two bits at a time. The same is also true for computing in the quantum regime. The three most important single-qubit gates are the NOT, Z, and Hadamard gate. In terms of a polarization qubit, these gate operations correspond to certain rotations in the Bloch sphere*. For a two-qubit gate, a control and target qubit are taken as inputs. An unitary operation is then performed on the target qubit depending on the state of the control qubit. By far the simplest of such two-qubit gates is the controlled-NOT (CNOT) gate. Cur-

*A Bloch sphere is a geometrical representation of the pure state space of a two-level quantum mechanical system.

rent research effort in this area focuses on the improvement of the performance of these quantum gates and on the implementation various schemes [54, 55, 56] that will make their operation fault-tolerant. These experimental implementations [57, 58, 59] require high quality polarization-entangled multi-photon states in order to achieve high fidelity to their expected theoretical operation.

For data communications between classical computers in a network, repeaters are sometimes used to boost the data signal as they become weaker during propagation. The quantum repeater serves an analogous function for the transmission quantum information. For example, in a long optical fiber-based cryptographic link, repeaters can be placed at regular intervals to ensure that there is no significant increase in the final key error rate due to losses in the fiber or decoherence. An intricate part of such a quantum repeater is an entanglement swapping or essentially quantum teleportation* operation. There have been numerous experimental studies on entanglement swapping [60, 61, 62, 63]. The photon pairs in these experiments are often generated by down-conversion of ultrafast optical pulses [64] so that they are tightly localized in time, giving rise to a higher probability of swapping events. As with the previous example, the fidelity of the operation is highly dependence on the entanglement quality of the multi-photon state mediating it.

1.2.4 Fundamental Tests of Quantum Physics

Apart from direct applications that use these photonic qubit states, they can also be used to conduct various fundamental tests of quantum physics.

One example where these photonic qubit states can be used is in the study of the optimality of various quantum tomography† schemes [15, 65, 66]. In experiments [65, 67, 68], state tomography is often used to characterize various systems involving single photon or entangled-photon pair state. However, little is done to establish the relative performance of various tomography schemes especially for photonic states with more than two photons. Findings from these experimental studies will help us develop more

*Quantum teleportation, or entanglement-assisted teleportation, is a technique used to transfer information on a quantum level, usually from one particle (or series of particles) to another particle (or series of particles) in another location via quantum entanglement.

†Quantum tomography is the practical estimation of quantum states through a fixed set of projective measurement on a large number of copies.

efficient quantum tomography schemes for use in various diagnostic procedures and even in tomography-based QKD protocols [69, 70].

These photonic qubit states can also be used to characterize the behaviors of various entanglement witnesses. Entanglement witnesses like Bell inequality [33] or CHSH inequality [34] are formulated to distinguish an entangled state from a separable one. The degree of violation of these inequalities depends heavily not only on the quantum state being tested and the amount of noise present, but also how the inequalities are formulated. Since then, the trend in this area of research has been the development of more generalized Bell inequalities [13, 71, 72, 73] that can be applied to quantum systems of arbitrarily high dimensionality and at the same time more resistant to noise.

1.3 Motivations For a High Quality Polarization-Entangled Multi-Photon Source

Research in the field of quantum information and quantum computation are beginning to branch into areas where experiments need to generate and manipulate multi-photon states with more than two photons. This is mainly driven by the needs of various applications where the benefits of moving over to larger quantum systems become significant.

One commonly implemented way of generating such entangled multi-photon states is by the SPDC of ultrafast optical pulses. Due to higher instantaneous power of these ultrafast optical pulses as compared to continuous-wave (cw) pump light, the higher-order processes in SPDC by which these multi-photon states are generated can be accessed. However, the inherently broad bandwidth of these ultrafast optical pump pulses brings with it a set of problems. The different dispersions encountered by the down-converted components results in spectral distinguishability between them which lowers the quality of polarization entanglement.* Thus in order to obtain a high quality polarization-entangled multi-photon source, this issue must first be addressed.

Therefore in the following chapter, I will start by briefly explaining the theory be-

*It should be noted that experiments involving SPDC processes pumped by ultrafast optical pulses in order to produce photon pairs that are tightly localization in time [8, 74] are also susceptible to this problem of spectral distinguishability.

hind SPDC before going in depth into various aspects of the setting up of a polarization-entangled four-photon source. This is followed by an experimental study of the spectral distinguishability in the down-converted components induced by the broadband pump in Chapter 3. Details on the implementation and experimental study into the spectral compensation scheme first proposed and implemented by Kim *et al.* [1] are presented in Chapter 4. In Chapter 5, I will present an experiment violating the spin-1 CHSH inequality before ending with some final remarks about the remaining issues limiting the entanglement quality in Chapter 6.

Chapter 2

Generation and Characterization of Polarization-Entangled Photons from Pulsed SPDC

The very first experiment involving an entangled state (Fig. 2.1) was implemented by C. A. Kocher and E. D. Commins in 1967 [3]. It used the process of atomic cascade in Ca (Fig. 2.2) to generate correlated photon pairs. In this experiment, ultraviolet light from a H_2 arc lamp is used to excite a beam of Ca atoms from the ground state $4s^2\,{}^1S_0$ to the excited state $3d4p\,{}^1P_1$. Through spontaneous decay, the Ca atoms then drop to the desired $4p^2\,{}^1S_0$ level. Each Ca atom then de-excites via the $4p4s\,{}^1P_1$ level back to the ground state producing a 551.3 nm and 422.7 nm photon in the process. As there is no net change in the total angular momentum J of the atom in the initial and final state, the photon pairs carry no net angular momentum. This, coupled with the fact that both the initial and final levels have the same even parity means that the emitted photons in each pair will exhibit polarization correlation. The experiment successfully showed the polarization correlation by recording the coincidence counts between the photons for various coincidence time windows* behind parallel and crossed polarizers. In the early 1980s using similar techniques, Alain Aspect *et al.* [2, 36, 37] successfully

*The coincidence time window is defined as the time after a single detection event within which a second single detection event can be considered coincident with it.

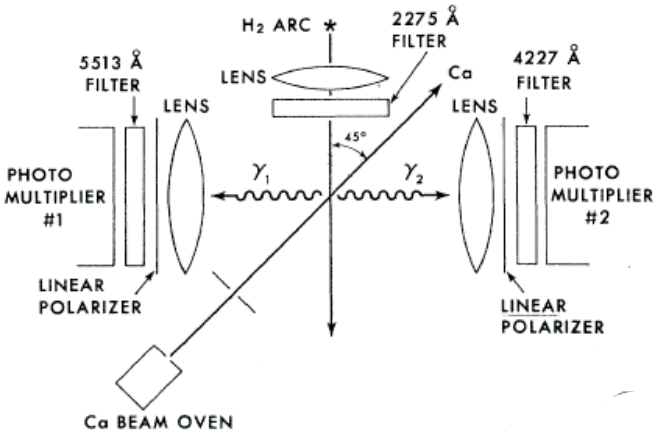

Figure 2.1: The experimental setup used by Kocher *et al.* in 1967 to generate polarization-correlated photon pairs. Ultraviolet light from a H_2 arc lamp excites a beam of Ca atoms. Polarization-correlated photon pairs are generated when the excited Ca atoms decay back to the ground state via an intermediate level (Fig. 2.2). These photon pairs then pass through linear polarizers followed by narrow-band interference filters to be detected by photomultiplier tubes. (Figure adapted from [3].)

implemented a source of polarization-entangled photon pairs that is able to violate the Bell inequality by up to 9 standard deviations.

In a parallel development, significant progress has been made in the field of nonlinear optics. This resulted in the first experimental implementation of a photon pair source (Fig. 2.3) based on the nonlinear optical effect of spontaneous parametric down-conversion (SPDC) by D. C. Burnham and D. L. Weinberg [4] in 1970. SPDC is still routinely used in experiments to generate photon pairs that are entangled in various degrees of freedom up to this very day.

These experiments normally use this process in two different regimes depending on the properties of the pump source. With continuous-wave (cw) pump light, bright sources of photon pairs in maximally entangled states with high fidelity in various degrees of freedom [22, 24] can be implemented. These sources are suitable for various applications such as quantum key distribution [75] and fundamental tests of quantum physics (e.g. tests of Leggett models [10, 76]).

However, for applications where photon pairs need to exhibit tight localization

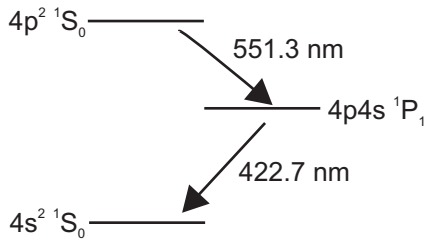

Figure 2.2: The atomic cascade of Ca. Each Ca atom de-excites from the excited $4p^2\,{}^1S_0$ level via the $4p4s\,{}^1P_1$ back to the ground state producing a 551.3 nm and 422.7 nm photon. The emitted photon pair does not carry any net angular momentum as $J = 0$ for both the initial and final states of the cascade. Coupled with the fact that both levels have the same even parity, the photons in each pair will exhibit polarization correlation.

in time [8, 23, 74], or when more than one pair should be simultaneously generated [62, 64, 77], the SPDC process needs to be pump by short optical pulses. In the following sections, I will begin by briefly describing the nonlinear optical effects of second harmonic generation (SHG) and SPDC. Then I will detail the implementation a of polarization-entangled multi-photon source followed by measurements used to assess its quality of polarization entanglement.

2.1 Second-order Nonlinear Optical Phenomena

To understand the origin of the various second-order nonlinear optical phenomena, we start by looking at the behaviors of the electrons and positively charged nuclei of the atoms in a dielectric material when subjected to an electric field of a light wave. The electric field causes a redistribution of the charges within the atoms, causing them to be polarized. Each atom then acquires a small dipole moment that is aligned to the direction of the applied electric field. In the regime where the applied electric field of the light wave is weak, the response of the dielectric material is linear with the applied electric field. This behavior can be written as

$$\boldsymbol{P} \approx \epsilon_0 \chi \boldsymbol{E}, \tag{2.1}$$

where $\boldsymbol{P}$ is the electric polarization (dipole moment per unit volume) induced in the dielectric, ϵ_0 is the electric permittivity of free space, χ is the linear electric susceptibil-

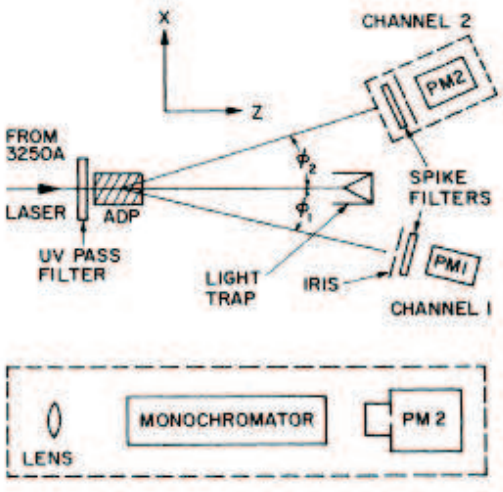

Figure 2.3: The first photon pair source based on the process of SPDC was implemented by Burnham *et al.* in 1970. An ADP crystal is pumped by a 325 nm beam from a He-Cd laser. The ADP crystal is cut in such a way that the optical axis makes an angle of 52.4° with the normal of the faces to satisfy the condition of phase matching. The down-converted photons then pass through a combination of spatial (iris) and spectral filtering (spike filter consisting of a monochromator) to be detected with the photomultiplier (PM) tubes. (Figure adapted from [4].)

Figure 2.4: Feynman diagrams for second-order nonlinear processes. (a) Second harmonic generation or frequency doubling. Two pump photons of the same frequency ω get annihilated producing an output photon of frequency 2ω. (b) Down-conversion. A pump photon of frequency ω_p gets annihilated producing two photons at the signal and idler frequencies w_p and w_i, respectively. The sum of the signal and idler frequencies w_p and w_i is equal the pump photon frequency ω_p.

ity, and $\boldsymbol{E}$ is the applied electric field. The susceptibility χ is related to the refractive index of the dielectric material. For an isotropic medium, the susceptibility χ only has one value. However, for a crystalline material, the susceptibility χ is a tensor quantity related to the symmetry of the crystal structure.

When large electric field amplitudes like those found in the output of some lasers are applied, higher-order contributions become significant. The linear behavior described by Eq. 2.1 needs to be modified with additional terms

$$P_i = \epsilon_0 \chi_{ij}^{(1)} E_j + \epsilon_0 \chi_{ijk}^{(2)} E_j E_k + ... + \epsilon_0 \chi_{ijk...l}^{(n)} E_j E_k ... E_l, \tag{2.2}$$

where $i, j, ..., k \in (1, 2, 3)$ and $\chi^{(n)}$ is the nth-order susceptibility. For the purpose of this thesis, we will be focusing on optical effects induced by the second-order susceptibility $\chi^{(2)}$. The susceptibility $\chi^{(2)}$ is responsible for various three-wave mixing processes*. The two processes of particular interest to us (Fig. 2.4) are second harmonic generation (SHG) or frequency doubling and spontaneous parametric down-conversion (SPDC).

2.1.1 Second Harmonic Generation (SHG)

In the process of SHG (Fig. 2.4a), two pump photons of the same frequency ω get annihilated producing an output photon of frequency 2ω. This is a special case of the process of sum frequency mixing where the two pump photons can be at different frequencies and the output photon has a frequency equal to the sum of the two frequencies of the pump photons.

*A brief introduction of the various three-wave mixing processes can be found in [49].

The process of SHG essentially can be understood as the modulation of the refractive index of the dielectric medium by an incoming electric field of a light wave. This modulation is coupled to the electric field through the susceptibility $\chi^{(2)}$. The effect of this modulation in the material is to create sidebands of various frequencies which are the sum and differences of the pump frequencies.

2.1.2 Spontaneous Parametric Down-conversion (SPDC)

In the process of SPDC (Fig. 2.4b), a pump photon of frequency ω_p gets annihilated producing a signal and idler* photon at frequency w_s and w_i, respectively. The term parametric in SPDC means that the down-conversion medium is left unchanged by the process. Thus, this necessarily means that a series of conservation laws must satisfied by the pump, signal, and idler photons. The conservation laws [79] are

$$\omega_p = \omega_s + \omega_i, \tag{2.3}$$

$$\overrightarrow{k_p} = \overrightarrow{k_s} + \overrightarrow{k_i}, \tag{2.4}$$

where Eq. 2.3 and Eq. 2.4 are known as the frequency matching condition and phase matching condition, respectively. The wavevectors in Eq. 2.4 which are in the form $\overrightarrow{k}_j$ can be expressed as

$$\overrightarrow{k_j} = \frac{n_j(\omega_j)\omega_j}{c}\hat{s}_j, \tag{2.5}$$

where $n_j(\omega_j)$ is a dispersive refractive index of a material dependent on ω_j, $\hat{s}_j$ is the unit vector pointing in the $\overrightarrow{k_j}$ direction, and c is the speed of light. This dependence of the wavevector $\overrightarrow{k}_j$ on the refractive index $n_j(\omega_j)$ allows us to rewrite Eq. 2.4 into

$$n_p(\omega_p)\omega_p\hat{s}_p = n_s(\omega_s)\omega_s\hat{s}_s + n_i(\omega_i)\omega_i\hat{s}_i. \tag{2.6}$$

If we now consider the special case for an isotropic medium, i.e. $n_p = n_s = n_i = n$ and degenerate down-conversion, i.e. $\omega_s = \omega_i = \frac{\omega_p}{2}$, the minimal magnitude of $|\overrightarrow{k_s}| + |\overrightarrow{k_i}|$ that can still satisfy the condition of momentum conservation (Eq. 2.4) occurs when the down-converted light is collinear with that of the pump. The expression in Eq. 2.6 then reduces to

$$n(\omega_p) = n(\frac{\omega_p}{2}). \tag{2.7}$$

*This naming convention has its origin in early research on optical parametric amplifiers [78] where only one of the two output modes (signal) is useful. The unused mode is called the idler.

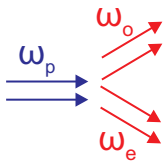

Figure 2.5: Feynman diagram for a second-order down-conversion process. With high intensity pump light there is higher probability where two pump photons get down-converted into two pairs of photons in close temporal proximity.

Since the refractive index n for most dielectric materials decreases with increasing frequency [78], both frequency and phase matching conditions cannot be simultaneously satisfied in an isotopic medium. To overcome this, there is a need for two channels into which the down-conversion can occur. This can be achieved in a birefringent medium, β-Barium-Borate (BBO) in our case, where there are two different refractive indices n_o and n_e for the ordinarily (o) and extraordinarily* (e) polarized light, respectively. The phase matching condition (Eq. 2.6) with a e-polarized pump can now be written in terms of n_o and n_e

$$n_e(\omega_p)\omega_p\hat{s}_p = n_e(\omega_e)\omega_e\hat{s}_e + n_o(\omega_o)\omega_o\hat{s}_o. \tag{2.8}$$

The down-conversion now result in photon pairs, each of which consists of an o and e-polarized photon.

Second-order down-conversion process (Fig. 2.5) in which two pump photons get down-converted into two pairs of photons in close temporal proximity can also occur. This is one of the main process by which multi-photon entangled states are generated. The rate of this double pair production increases quadratically with pump power [23]. This is in contrast with the pair production rate which increases linearly with the pump power [23]. Thus, the use of high intensity pump light will result in a higher probability for the generation of double pairs. This is the main justification for our use of femtosecond optical pulses, which have high instantaneous intensity, for pumping the down-conversion in the later experiments.

However, there is a major drawback when it comes to implementing a down-conversion source in such a pulsed regime. Due to the difference in n_o and n_e, the

*The term "ordinary" and "extraoridnary" refers to the slow and fast axis of a birefringent crystal, respectively.

o and e-polarized down-converted light will experience different amount of dispersion in the birefringent medium. This induces a difference in the bandwidth of the spectral distributions of the o and e-polarized light. As we will see in Chapter 3, this spectral difference between the components of the down-converted light is ultimately responsible for the degraded polarization entanglement quality often associated with such a pulsed configuration.

2.2 Generation of Polarization-Entangled Photons with SPDC

There are two of types of phase matching, type-I and type-II, differentiated by whether the signal and idler photon within each pair have the same or orthogonal polarization. For the purpose of this thesis, we will be focusing on the specific case of type-II phase matching (Fig. 2.6). In type-II phase matching, an e-polarized pump photon gets down-converted into a pair of o and e-polarized photons of lower energy. The o and e-polarized photons are emitted from the down-conversion crystal in two respective cones which are non-concentric with either the pump beam or each other. In our setup, the down-conversion crystal is oriented in such a way that the extraordinary axis coincides with the vertical (V) polarization, while the ordinary axis coincides with the horizontal (H) polarization. I will denote these two cases as V_e and H_o, respectively.

In the previous section, I have indicated that the difference in the dispersion experienced by the o and e-polarized light will induce a difference in their spectral bandwidth. Thus, the label o and e now serve to describe the spectral bandwidth of down-converted photons instead. It should be noted that since the spectral bandwidths of the down-converted photons are independent of their polarizations, the label o and e will be left unchange by any rotation operation. Any rotation transformation will only affect the polarization label H and V.

For polarization-entangled photon pairs, we need two possible decay paths given by the polarization combinations $|H\rangle|V\rangle$ and $|V\rangle|H\rangle$. This situation can only be found at the two intersections of the e and o emission cones, which also define two spatial modes 1 and 2. This is called a "crossed-ring" configuration* [7, 82]. The quantum

*Down-conversion setups can also be implemented in the "beamlike" [80] and collinear [81] config-

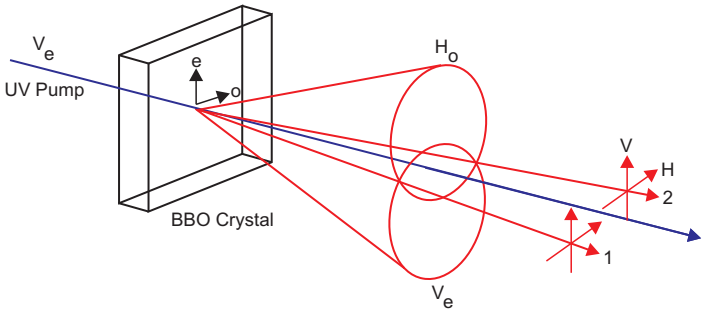

Figure 2.6: Type-II phase matched down-conversion. In type-II phase matching, an e-polarized pump photon gets down-converted into a pair of o and e-polarized photons of lower energy. The o and e-polarized photons are emitted from the down-conversion crystal in two respective cones which are non-concentric with either the pump beam or each other. In our setup, the down-conversion crystal is oriented in such a way that the extraordinary axis coincides with the vertical (V) polarization, while the ordinary axis coincides with the horizontal (H) polarization. These two cases are denoted as V_e and H_o, respectively.

mechanical creation operator for the two-photon polarization state describing such a situation can be written as

$$|\Psi\rangle \;=\; C(a^{\dagger}_{H_o} b^{\dagger}_{V_e} + e^{i\delta} a^{\dagger}_{V_e} b^{\dagger}_{H_o})|0\rangle, \tag{2.9}$$

where C is the normalization constant, $a^{\dagger}_i$ and $b^{\dagger}_i$* are the creation operators of a photon with polarization state i in spatial mode 1 and 2, respectively. After normalization, the following polarization-entangled two-photon state is obtained

$$|\Psi\rangle = \frac{1}{\sqrt{2}} \left(|H_o\rangle_1 |V_e\rangle_2 \;+\; e^{i\delta} |V_e\rangle_1 |H_o\rangle_2 \right) . \tag{2.10}$$

For the second-order down-conversion process, the creation operator is simply the square of the operator in Eq. 2.9

$$|\Psi\rangle^{(2)} \;=\; C^2(a^{\dagger}_{H_o} b^{\dagger}_{V_e} + e^{i\delta} a^{\dagger}_{V_e} b^{\dagger}_{H_o})^2|0\rangle. \tag{2.11}$$

After normalization, the following four-photon polarization state for the second-order

uration.

*Such a representation of the number of photons with a specific polarization in each spatial mode is called a Fock state. The creation operator $a^{\dagger}$ obeys the relation, $a^{\dagger}|n\rangle = \sqrt{n+1}|n+1\rangle$.

down-conversion is obtained

$$|\Psi\rangle^{(2)} = \frac{1}{\sqrt{3}}(|H_oH_o\rangle_1|V_eV_e\rangle_2 + e^{i\delta}|H_oV_e\rangle_1|H_oV_e\rangle_2 + e^{i2\delta}|V_eV_e\rangle_1|H_oH_o\rangle_2). \quad (2.12)$$

2.2.1 Compensation of Temporal and Transverse Walkoffs

In actuality, the photon pairs at the intersection of the o and e emission cone (Fig. 2.6) are not in a pure polarization-entangled state (Eq. 2.10). The different refractive index n_o and n_e of the birefringent crystal result in a difference in the propagation velocity of the o and e wave in the crystal. This gives rise to a relative delay between the arrival time of the o and e-polarized photon in each pair that is dependent on the site in the crystal where they are created. In one extreme case (Fig. 2.7a), the photon pairs are created at the face of the crystal incident to the pump beam. This give rise to the maximal time difference between the arrival time of the o and e-polarized photon at the detectors. In the other extreme (Fig. 2.7b), the photon pairs are created at the face where the pump exits the crystal. Thus, there is no relative delay between the o and e-polarized photons. Only the photon pair combinations $|H_o\rangle_1|V_e\rangle_2$ and $|V_e\rangle_1|H_o\rangle_2$ created here are truly indistinguishable and exist in a pure polarization state. However, when the photon pairs from all the creation sites are included, a mixed state is produced resulting in a lower polarization entanglement quality. It should be noted that this problem of temporal distinguishability between the photon pairs is not eliminated simply by having a coincidence time window to be greater than the maximal relative delay expected. This is due to the fact that entanglement, in the context used here, is a process involving two-photon interference between the two Feynman alternatives creating the $|H_o\rangle_1|V_e\rangle_2$ and $|V_e\rangle_1|H_o\rangle_2$ combination. Thus, any distinguishability of the two decay paths in degrees of freedom that are not monitored or resolved will still manifest itself in the result of certain measurement.

A common way to eliminate this problem [7] involves the use of a combination of half-wave plates ($\lambda/2$) and compensation crystals (CC) (Fig. 2.7). The photons first pass through a $\lambda/2$ which rotates their polarization by 90°. This is followed by CC which are identical to the crystal used for down-conversion except with half the thickness. The optical axis (OA) of both CC are aligned in the same direction as that of the down-conversion crystal. In the first extreme case (Fig. 2.7a), the CC will halve the relative delay between the photons in the pair. In the second extreme case (Fig. 2.7b), the CC

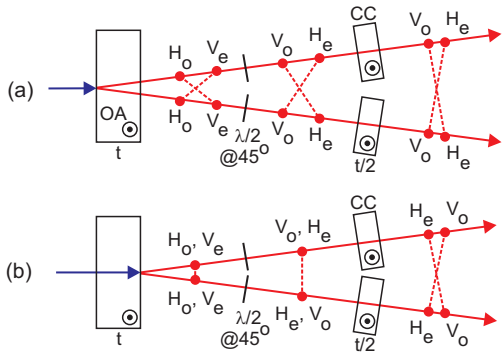

Figure 2.7: Compensation of temporal walkoff. The photons first pass through a $\lambda/2$ which rotates their polarization by 90°. This is followed by CC which are identical to the crystal used for down-conversion except with half the thickness. The optical axis (OA) of both CC are aligned in the same direction as that of the down-conversion crystal. In the first extreme case (a), the CC will halve the relative delay between the photons in the pair. In the second extreme case (b), the CC will induce a relative delay equal to that in the previous case between the photons in the pair. Thus, the photons pairs from these two cases are indistinguishable in the temporal degree of freedom, resulting in a pure polarization-entangled state. This is also true for all complementary creation sites in the crystal symmetric about the center of the crystal. For photon pairs created right in the center of the down-conversion crystal, the relative delay is just eliminated by the CC.

will induce a relative delay equal to that in the previous case between the photons in the pair. Thus, the photons pairs from these two cases are indistinguishable in the temporal degree of freedom, resulting in a pure polarization-entangled state. This is also true for all complementary creation sites in the crystal symmetric about the center of the crystal. For photon pairs created right in the center of the down-conversion crystal, the relative delay is just eliminated by the CC. The compensation stage involves a rotation of the polarization of the down-converted photons by 90°. Thus, the two and four-photon polarization state in Eq. 2.10 and Eq. 2.12 is now rewritten as

$$|\Psi\rangle = \frac{1}{\sqrt{2}}\left(|H_e\rangle_1|V_o\rangle_2 + e^{i\delta}|V_o\rangle_1|H_e\rangle_2\right), \tag{2.13}$$

$$|\Psi\rangle^{(2)} = \frac{1}{\sqrt{3}}(|H_eH_e\rangle_1|V_oV_o\rangle_2 + e^{i\delta}|H_eV_o\rangle_1|H_eV_o\rangle_2 + e^{i2\delta}|V_oV_o\rangle_1|H_eH_e\rangle_2), \tag{2.14}$$

respectively.

Apart from eliminating the problem of temporal distinguishability, the CC are also used to compensate for the transverse walkoff (Fig. 2.8) between the down-converted o and e-polarized light. To satisfy the phase matching condition in Eq. 2.4, the axis perpendicular to both the fast and slow axis of the down-conversion crystal is usually titled at an vertical angle to the pump beam. This results in a slightly different profile for the o and e emission cones. At each of the intersection of the emission cones, this will appear as an elongated spread of the o-polarized photon distribution as compared to that of the e-polarized photons (Fig. 2.8). After passing through the $\lambda/2$, the polarization of the photons are rotated by 90°. The CC, which are orientated such that their OA are parallel to that of the down-conversion crystal, then cause a shift in the path of the down-converted light such that the center for the distribution of the o and e-polarized photons coincide. This provide better overlap between the two distributions and thus results in a better spatial mode for collection into single mode optical fibers.

The vertical angle between the fast axis of the CC and the down-converted light beam can be adjusted by tilting the CC. This changes the relative phase between the H_e and V_o photons in each of the spatial mode. Therefore, the CC also allow us to adjust the free phase δ (Eq. 2.10) so that different entangled two-photon polarization state can be generated. When the free phase δ is adjusted to $\delta = \pi$, the two and

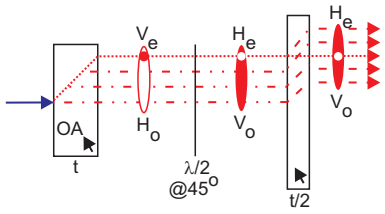

Figure 2.8: Compensation of transverse walkoff. At each of the intersection of the emission cones, there is an elongated spread of the o-polarized photons as compared to the e-polarized photons (Fig. 2.8). After passing through the $\lambda/2$, the polarization of the photons are rotated by 90°. The CC, which are orientated such that their OA are parallel to that of the down-conversion crystal, then cause a shift in the path of the down-converted light such that the center for the distribution of the o and e-polarized photons coincide. This provide better overlap between the two distributions and thus results in a better spatial mode for collection into single mode optical fibers.

four-photon polarization state in Eq. 2.13 and Eq. 2.14 are rewritten as

$$|\Psi^-\rangle = \frac{1}{\sqrt{2}}\left(|H_e\rangle_1|V_o\rangle_2 - |V_o\rangle_1|H_e\rangle_2\right), \tag{2.15}$$

$$|\Psi^-\rangle^{(2)} = \frac{1}{\sqrt{3}}(|H_eH_e\rangle_1|V_oV_o\rangle_2 - |H_eV_o\rangle_1|H_eV_o\rangle_2 + |V_oV_o\rangle_1|H_eH_e\rangle_2), \tag{2.16}$$

respectively.

2.3 Characterization of Polarization-Entangled Photons

There are a number of measures for entanglement quality [83, 84] of quantum states. These measures often require a full characterization of the quantum state of the system being investigated to establish those quantities. The sometimes experimentally complicated or numerous measurements required for such a full characterization of a quantum system coupled with need for significant post-processing of the acquired data means that such measures may not always be possible or practical. For example, to optimize the alignment of the type of down-conversion source mentioned in Section 2.2, one may need to perform numerous iterations of making small adjustments to the source followed by monitoring the quality of polarization-entanglement between the photons under these alignments. In such a case a full characterization of the source may not

be practical. What is needed here is an experimentally simple and fast measurement that can be carried out to gain an idea of the quality of entanglement between photons generated by the source. A common method that fits these criteria are the visibility measurements. These measurements are normally carried out in the H/V and +45°/-45° bases. We will be relying on these measurement of visibilities to characterize our source polarization-entangled photons in the coming chapters.

2.3.1 Derivation of Joint Detection Probability for Polarization-Entangled States

Various methods used for characterizing polarization-entangled sources, e.g. visibility measurements, quantum state tomography [15, 65, 66], and violation of Bell inequalities [13, 33, 34], involve the joint detection of the down-converted photons after they have been projected onto various polarization bases. In order for us to better interpret the results from such measurements and to fit them to the available theoretical models, we need to derive analytical expressions describing the expected joint detection probability for any measurement basis given various polarization-entangled states.

For the purpose of this thesis, we will be presenting only a few of the cases where the joint detection probabilities of measurements involve projection of the down-converted photons onto linear polarization bases. Such projections can be implemented in a polarization analyzer consisting of a rotatable half-wave plate ($\lambda/2$) followed by a polarizing beam splitter (PBS). It should be noted that a rotation of the $\lambda/2$ by an angle $\alpha/2$ will cause an effective rotation of the basis by angle α. For simplicity, for the rest of this thesis, we will only refer to the effective rotation of the measurement basis.

We begin by considering the case of single-photons. In the Jones vector notation*, the two single-photon basis polarization states $|H\rangle$ and $|V\rangle$ are given by the column vectors

$$|H\rangle = \begin{pmatrix} 1 \\ 0 \end{pmatrix}, |V\rangle = \begin{pmatrix} 0 \\ 1 \end{pmatrix}, \tag{2.17}$$

respectively. A rotation matrix $R(\alpha)$, describing a clockwise rotation of angle α is

*It should be noted that the Jones vector notation is only valid for pure polarization states. For mixed polarization states, the Stokes vector notation needs to be applied.

represented by the transformation matrix

$$R(\alpha) = \begin{pmatrix} \cos\alpha & -\sin\alpha \\ \sin\alpha & \cos\alpha \end{pmatrix}. \tag{2.18}$$

Thus, to detect a photon linearly polarized in a direction at a clockwise angle α from horizontal, which we denoted as $|H\rangle'$, through a polarization filter transmitting $|H\rangle$, a rotation of angle $-\alpha$ must first be performed on $|H\rangle'$. The analyzer now have the measurement basis

$$R(-\alpha)|H\rangle = \begin{pmatrix} \cos\alpha \\ -\sin\alpha \end{pmatrix}. \tag{2.19}$$

The probability of detection given any arbitrary pure polarization state $|\psi\rangle$ with this configuration is then given by

$$P(H|\alpha) = |\langle H|R(-\alpha)|\psi\rangle|^2 \tag{2.20}$$

This can be easily extended to the two-photon polarization states. In this increased polarization space, there are four two-photon polarization bases given by $|H\rangle_1|H\rangle_2$, $|H\rangle_1|V\rangle_2$, $|V\rangle_1|H\rangle_2$, and $|V\rangle_1|V\rangle_2$. The Jones vector notation describing the basis state $|H\rangle_1|H\rangle_2$ for example, is given by

$$|H\rangle_1|H\rangle_1 = \begin{pmatrix} 1 \\ 0 \end{pmatrix} \otimes \begin{pmatrix} 1 \\ 0 \end{pmatrix} = \begin{pmatrix} 1 \\ 0 \\ 0 \\ 0 \end{pmatrix} \tag{2.21}$$

We can define a two-photon transformation matrix written as

$$R^{(2)}(\alpha,\beta) = R(\alpha) \otimes R(\beta), \tag{2.22}$$

where $R(\alpha)$ and $R(\beta)$ are the transformation performed in spatial mode 1 and 2, respectively. Thus, the joint detection probability of obtaining the measurement result $|H\rangle_1|H\rangle_2$ with analyzer settings α and β, respectively for the input state $|\Psi^-\rangle$ (Eq. 2.15) is given by

$$\begin{aligned} P(H,H|\alpha,\beta) &= |\langle H|_1\langle H|_2 R(-\alpha,-\beta)|\Psi^-\rangle|^2 \\ &= \frac{1}{2}\sin^2(\alpha-\beta). \end{aligned} \tag{2.23}$$

Applying the same procedure for the four-photon polarization states, we will obtain sixteen polarization bases. In anticipation of the analyzer setup implemented for the

violation of the spin-1 CHSH inequality presented in Chapter 5, we can define a four-photon transformation matrix given by

$$R^{(4)}(\alpha,\beta) \;=\; R(\alpha)\otimes R(\alpha)\otimes R(\beta)\otimes R(\beta), \tag{2.24}$$

where the same transformation is applied to both photons in each of the two spatial modes. Thus, the joint detection probability of obtaining the measurement result $|HH\rangle_1|HH\rangle_2$ with analyzer settings α and β, respectively for the input state $|\Psi^-\rangle^{(2)}$ (Eq. 2.16) is given by

$$\begin{aligned} P(HH,HH|\alpha,\beta) &= |\langle HH|_1\langle HH|_2 R^{(4)}(-\alpha,-\beta)|\Psi^-\rangle^{(2)}|^2 \\ &= \frac{1}{3}\sin^4(\alpha-\beta). \end{aligned} \tag{2.25}$$

2.3.2 Visibility Measurements in the H/V and +45°/-45° Bases

To understand how visibilities in the H/V and +45°/-45° bases are related to quality of polarization entanglement, we start by considering one of the maximally entangled Bell states

$$|\Psi^-\rangle = \frac{1}{\sqrt{2}}\left(|H\rangle_1|V\rangle_2 \;-\; |V\rangle_1|H\rangle_2\right). \tag{2.26}$$

Since the $|\Psi^-\rangle$ state is rotationally invariant, it is left unchanged by a coordinate transformation to the +45°/-45° basis, i.e.

$$|\Psi^-\rangle = \frac{1}{\sqrt{2}}\left(|+\rangle_1|-\rangle_2 \;-\; |-\rangle_1|+\rangle_2\right), \tag{2.27}$$

where + and - denotes the +45° and -45° polarization, respectively.

The simplest definition of the visibilities measured in the H/V and +45°/-45° bases, denoted as V_{HV} and V_{45} respectively, can be written as

$$V_{HV} \;=\; \frac{|C_{VH} \;-\; C_{VV}|}{C_{VH} \;+\; C_{VV}}, \tag{2.28}$$

$$V_{45} \;=\; \frac{|C_{+-} \;-\; C_{++}|}{C_{+-} \;+\; C_{++}}, \tag{2.29}$$

where C_{ij} is the number of coincidences obtained when the down-converted photons in spatial mode 1 and 2 are projected onto polarization i and j, respectively. Thus, it can seen for the $|\Psi^-\rangle$ states in Eq. 2.26 and Eq. 2.27, both quantities V_{HV} and V_{45} will have the value of 1 as there is no contribution giving rise to coincidences for correlated analyzer settings.

For a more realistic description of the polarization state of entangled photons generated from SPDC, noise contributions need to be included. Regardless of the cause that is lowering the quality of polarization entanglement, they can be written as either a colored noise ($\rho_{colored}$) or white noise (ρ_{white}) contribution. These are given by

$$\rho_{colored} = \frac{1}{2}(|H\rangle_1|V\rangle_2\langle H|_1\langle V|_2 \quad + \quad |V\rangle_1|H\rangle_2\langle V|_1\langle H|_2), \tag{2.30}$$

$$\begin{aligned}\rho_{white} = \frac{1}{4}(&|H\rangle_1|H\rangle_2\langle H|_1\langle H|_2 \quad + \quad |H\rangle_1|V\rangle_2\langle H|_1\langle V|_2 \\ &+|V\rangle_1|H\rangle_2\langle V|_1\langle H|_2 \quad + \quad |V\rangle_1|V\rangle_2\langle V|_1\langle V|_2).\end{aligned} \tag{2.31}$$

The colored noise contribution $\rho_{colored}$ consists only of terms found in the pure state $|\Psi^-\rangle$ (Eq. 2.26) itself. The white noise contribution ρ_{white} consists of terms involving all possible combination of coincidences between H and V-polarized photons. It should be noted that the contributions from each of the terms in the Eq.2.30 and Eq.2.31 are not equal in general. With the added noise, the system can now be described completely by a density matrix ρ consisting of a contribution from the pure state $|\Psi^-\rangle$ and a noise contribution ρ_{noise}

$$\rho = p|\Psi^-\rangle\langle\Psi^-| + (1-p)\rho_{noise}, \tag{2.32}$$

where p gives the relative contribution between the pure state $|\Psi^-\rangle$ and ρ_{noise}, which itself is a combination of $\rho_{colored}$ and ρ_{white}.

With colored noise contribution, it can be seen that V_{HV} will still be 1 due to the lack of a correlation term. However, with white noise contribution, V_{HV} will be lowered depending on the relative contribution p. This is due the presence of a correlation term in the white noise. When viewed in the 45°/-45° bases, both colored and white noise in the H/V bases will be manifested as white noise

$$\begin{aligned}\rho_{white} = \frac{1}{4}(&|+\rangle_1|+\rangle_2\langle+|_1\langle+|_2 \quad + \quad |+\rangle_1|-\rangle_2\langle+|_1\langle-|_2 \\ &+|-\rangle_1|+\rangle_2\langle-|_1\langle+|_2 \quad + \quad |-\rangle_1|-\rangle_2\langle-|_1\langle-|_2).\end{aligned} \tag{2.33}$$

This means V_{45} will be lowered with either contribution from colored or white noise in the H/V bases. Thus, to gain an idea of the type of noise present in a source of polarization-entangled photons and in turn the quality of entanglement between them, one needs to carry out measurement for both V_{HV} and V_{45}.

In the definition of visibility in Eq. 2.28 and Eq. 2.29, the coincidence counts at only two settings of the analyzer, i.e. correlation and anti-correlation, are used to evaluate

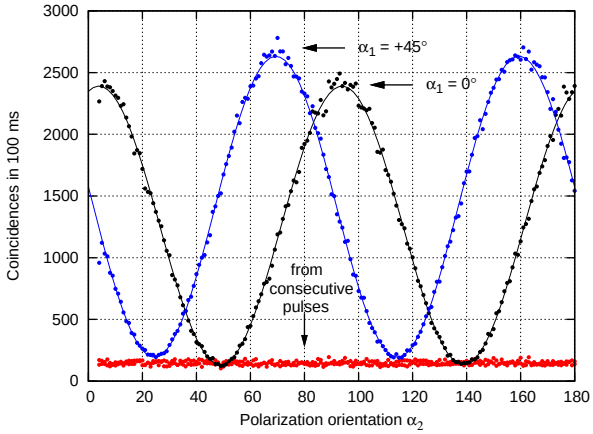

Figure 2.9: A typical polarization correlation measurement in the H/V and $+45°/-45°$ bases. The bottom trace represents pair coincidences from consecutive pulses.

the visibility. For the actual visibility measurements $V_{HV}(V_{45})$, the down-converted photon in one spatial mode is projected onto the $V(+45°)$ polarization while the other is projected onto a full range of linear polarizations. A sinusoidal function is then fitted to the trace of the recorded coincidences versus orientation of the analyzer. A typical curve is shown in Fig. 2.9. From the maximum and minimum of the fitted curve, the visibility can be obtained. As the visibility is now obtained by considering counts from a range linear polarization, this makes the visibility less prone to random error due to fluctuation in coincidence counts at each point. The orientation of the second analyzer where we will observe maximal visibility is dependent on the relative contribution of the decay paths. Thus, by scanning of the full range of linear polarizations, we can always evaluate the maximal visibility associated with the state being investigated.

With the steps presented in the previous section, we are able to calculate the expected values for visibilities V_{HV} and V_{45} for various relative contribution p between the pure state $|\Psi^-\rangle$ (Eq. 2.26) and ρ_{noise} (Fig. 2.10). From Fig. 2.10 we can see that for the case with colored noise contribution $\rho_{colored}$, only visibility V_{45} varies linearly with p while V_{HV} remains consistently high. However, with contribution from white noise ρ_{white}, both visibilities V_{HV} and V_{45} changes linearly with p. This shows that V_{45} is a better measure of the polarization entanglement quality .

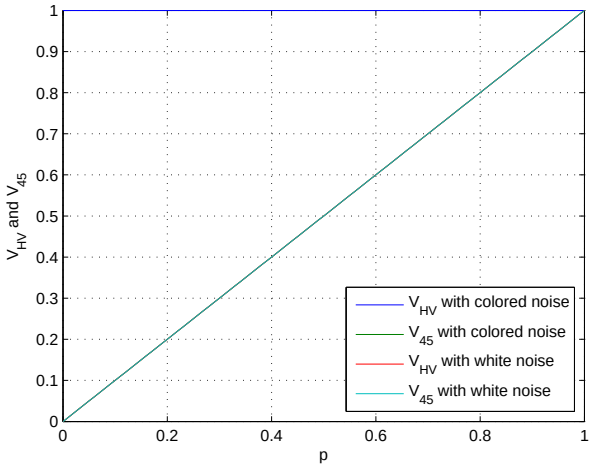

Figure 2.10: With the steps presented in the previous section, we obtained the dependence of V_{HV} and V_{45} on various relative contribution p between the pure state $|\Psi^-\rangle$ (Eq. 2.26) and ρ_{noise}. For the case with colored noise contribution $\rho_{colored}$, only visibility V_{45} varies linearly with p while V_{HV} remains consistently high. However, with contribution from white noise ρ_{white}, both visibilities V_{HV} and V_{45} changes linearly with p. This shows that V_{45} is a better measure of the polarization entanglement quality.

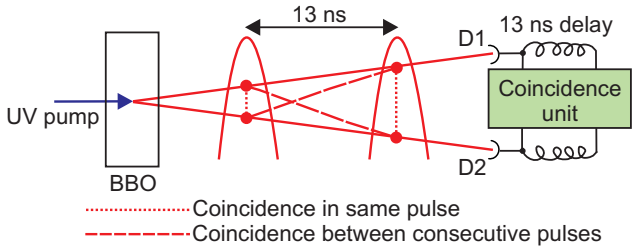

Figure 2.11: Electronic setup used to record pair coincidences between consecutive pulses. The signal from the passively quenched Silicon avalanche photodiodes (D1, D2) used to register single photon events are duplicated. One copy of the signal gets delayed by 13 ns; the period between output pulses from the femtosecond laser. Both non-delayed and delayed copies are then sent into a coincidence unit where all possible patterns of coincidences between the four inputs within a coincidence window shorter than the repetition period of the pump are recorded. Pair coincidences in the same pulse and between consecutive pulses can then be extracted.

2.3.3 Estimation of Higher-Order Contribution from Two-Photon Measurement

Due to the high instantaneous power involved in the femtosecond-pumped down-conversion, higher-order processes (mainly four-photon generation) become significant, and it is important to quantify their contribution. When observing only two-fold coincidences, this four-photon contribution will lead to uncorrelated events lowering the two-photon visibilities.

To estimate this four-photon contribution, we record the pair coincidences between consecutive pulses in the same run. This is done by the electronic setup shown in Fig. 2.11. The signal from the passively quenched Silicon avalanche photodiodes (D1, D2) used to register single photon events are duplicated. One copy of the signal gets delayed by 13 ns; the period between output pulses from the femtosecond laser. Both non-delayed and delayed copies are then sent into a coincidence unit where all possible patterns of coincidences between the four inputs within a coincidence window shorter than the repetition period of the pump are recorded. Pair coincidences in the same pulse and between consecutive pulses can then be extracted. The pair coincidences between consecutive pulses is shown as the red trace in Fig. 2.9.

Following an argument put forward in [85], the coincidence rate between consecutive pulses is the same as the rate of distinguishable pairs generated in the same pulse. If the two photon pairs are indistinguishable, the four-photon contribution to the two-photon coincidence rate will be half of the pair coincidence rate between consecutive pulses. Thus, from the recorded coincidences between consecutive pulses, we can come up with a lower and upper bound for the four-photon generation rate in the setup. This correction procedure will be applied to the various two-photon measurements in later chapters.

Chapter 3

Joint Spectrum Mapping of Polarization Entanglement in Ultrafast SPDC

Spontaneous parametric down-conversion (SPDC) has been widely used to generate entangled photons required in various quantum information protocols [86]. Typically, this process is used in two different regimes distinguished by the properties of the pump source. In some experiments, light from continuous-wave (cw) lasers is used to pump the SPDC process [4, 7, 87]. These sources can be very bright and provide photon pairs in maximally entangled states with high fidelity in various degrees of freedom [22, 24], making them suitable for applications such as quantum key distribution [75] and fundamental tests of quantum physics (e.g. tests of Leggett models [10, 76]).

The other regime covers experiments in which photon pairs need to exhibit tight localization in time [8, 23, 74], or when more than one pair should be simultaneously generated [62, 64, 77]. In such cases, short optical pulses with a coherence time compatible with that of the down-converted photons (on the order of few 100 fs) have to be used as a pump. The short pulse duration implies a wide distribution of pump frequencies. In combination with the dispersion relations of the nonlinear optical material this leads to entanglement of the polarization degree of freedom with the spectral properties of the down-converted photons [88]. For the purpose of generating pure entangled

states in only one variable, this is generally detrimental, manifesting itself as a degree of mixedness when only the polarization is considered (with the exception of the work reported in [9]). Thus, there is a strong interest in improving the quality and brightness of pulsed sources of polarization-entangled photons. While there are several proposals and demonstrations [1, 89, 90, 91, 92] based on spectral and temporal engineering to address the separation of spectral degrees of freedom, none of them has been widely adopted.

This chapter presents an experimental study of the influence of the spectral degree of freedom on polarization entanglement for traditional type-II SPDC sources in a femtosecond pulsed regime, e.g. as those used in experiments on teleportation [8] and entanglement swapping [60, 62]. By investigating the impact of joint spectral properties of SPDC on polarization entanglement, we complement recent experimental work [93, 94, 95].

3.1 Entanglement and spectral distinguishability

As in early experiments to entangle photon pairs in atomic cascade decays [2, 36, 37], the process of SPDC is able to generate polarization-entangled photons because two different decay paths result in two-photon states which are indistinguishable apart from their polarization degree of freedom. This can be seen from the simplest description of SPDC which is formulated in terms of three plane wave optical modes. The input corresponds to a narrow-band pump mode with a well defined wave vector $\overrightarrow{k_p}$, and output modes with wave vectors $\overrightarrow{k_s}$, $\overrightarrow{k_i}$ may be populated via down-conversion if phase matching conditions and energy conservation are fulfilled [87]:

$$\begin{aligned} \overrightarrow{k_p} &= \overrightarrow{k_s} + \overrightarrow{k_i} \\ \omega_p &= \omega_s + \omega_i \end{aligned} \tag{3.1}$$

In some birefringent materials, these conditions can be satisfied in two different ways, producing either an horizontally/vertically (H_1V_2) or a V_1H_2 polarized pair [7]. If the two processes are truly indistinguishable, a photon pair may be observed in a pure state:

$$|\Psi\rangle = \frac{1}{\sqrt{2}}\left(|H\rangle_1|V\rangle_2 + e^{i\delta}|V\rangle_1|H\rangle_2\right) \tag{3.2}$$

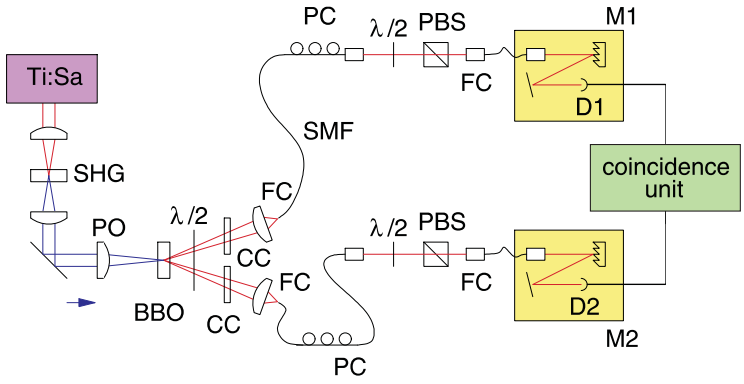

Figure 3.1: Schematic of the spontaneous parametric down-conversion (SPDC) setup. A femtosecond-pumped SPDC process generates photon pairs in single mode optical fibers which pass through polarization filters and subsequent grating monochromators.

For cw pumped down-conversion, this simple argument is enough to account for the presence of polarization entanglement and properties such as the bandwidth of down-converted photons [7, 25]. However, in a pulsed pump regime, the short duration of the pump imposes a Fourier limited spread of the input energy. Together with the broader phase matching conditions due to the difference in the dispersion relations for the ordinary (o) and extraordinary (e) waves in birefringent materials, this gives rise to spectral signatures which distinguish the two down-conversion processes. Leakage of polarization information into degrees of freedom which are not normally monitored results in mixedness of the polarization state of the photon pair. This effect of the spectral information can be observed by jointly measuring the spectral and polarization correlations between the down-conversion modes.

3.2 Experimental Setup

In order to perform spectrally resolved polarization correlation measurements on the down-converted photons, we implemented a photon pair source using traditional type-II phase matching in a crossed-ring configuration [7], followed by polarization analyzers and grating monochromators to resolve the different spectral components for both photons (Fig. 5.2).

The output of a Ti:Sapphire (Ti:Sa) laser* with central wavelength $\overline{\lambda}_c = 780\,\text{nm}$, pulse duration $\approx 150\,\text{fs}$, repetition rate 76 MHz, average power 1.1 W is frequency doubled (SHG) to produce optical pulses at $\overline{\lambda}_p = 390\,\text{nm}$. This light (average power 400 mW) passes through pump optics (PO) to correct for the astigmatism and to focus the beam down to a waist of $80\,\mu\text{m}$. At the focus, a 2 mm thick BBO crystal cut for collinear type-II phase matching ($\theta = 43.6°$, $\phi = 30.0°$) serves as the non-linear medium for down-conversion. The crystal is tilted such that the wavelength-degenerate decay path emerges at an approximate 3° from the axis of the 390 nm pump beam. A half-wave plate ($\lambda/2$) and a pair of compensation crystals (CC) take care of temporal and transversal walk-off† [7].

The spatial modes (spatial mode 1 and 2) of the down-converted photons, defined by single mode optical fibers (SMF), are matched to the pump mode to optimize the collection [25]. In type-II SPDC, each down-converted pair consists of one o and one e-polarized photon, and our setup is aligned such that ordinary corresponds to vertical (V), while extraordinary corresponds to horizontal (H) polarization after compensation. A pair of polarization controllers (PC) is used to ensure that the SMF do not affect the polarization of the collected photons. The free phase δ between the two decay possibilities in the polarization state Eq. 3.2 is adjusted to $\delta = \pi$ by tilting the CC to arrive at an approximate singlet Bell state $|\Psi^-\rangle$:

$$|\Psi^-\rangle = \frac{1}{\sqrt{2}} \left(|H\rangle_1 |V\rangle_2 - |V\rangle_1 |H\rangle_2 \right) , \tag{3.3}$$

which we will investigate for the rest of the chapter.

The polarization analysis in each arm is performed by a combination of another half-wave plate ($\lambda/2$) and a polarizing beam splitter (PBS), allowing projections onto any arbitrary linear polarization. We denote the direction of these linear polarizations by their rotation α_1 and α_2 with respect to vertical. The transmitted photons are transferred into grating monochromators on each arm (M1, M2) with 0.3 nm (FWHM) resolution and then detected with passively quenched Silicon avalanche photodiodes (D1, D2). Output of the two detectors is sent into a coincidence unit with a coincidence window shorter than the repetition period of the pump laser.

*For this setup, we are using a Mira-900 (Coherent) Ti:Sa laser pumped by 10 W of 532 nm light from a Verdi-V10 (Coherent) solid-state pump laser.

†Refer to Section 2.2.1 for details on how the temporal and transversal walk-offs are eliminated.

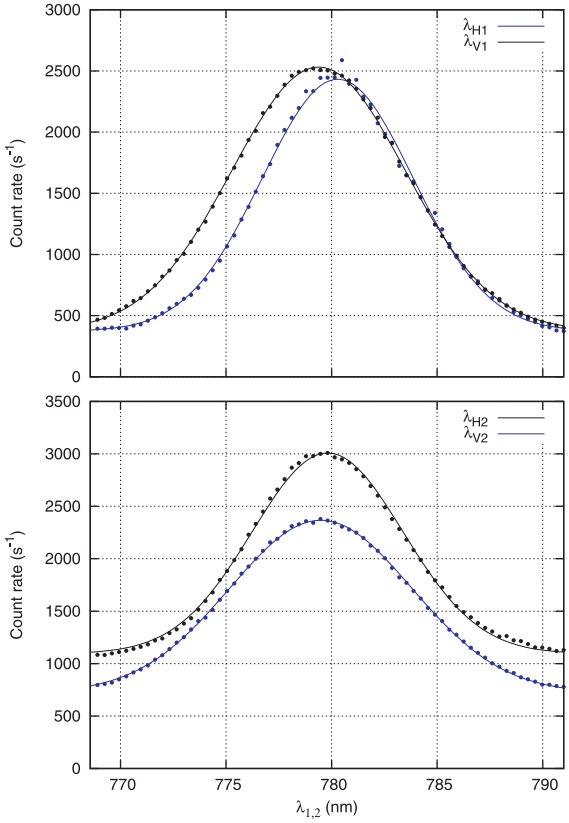

Figure 3.2: The spectral distribution of the photons in each of the down-conversion modes individually for both the spatial modes defined by the SMF. We obtained from a fit (solid traces) of the measured data (dotted traces) to a Gaussian distribution, central wavelengths of $\overline{\lambda}_{H1} \approx 780.3\,\text{nm}$ and $\overline{\lambda}_{V1} \approx 779.5\,\text{nm}$ for spatial mode 1 (upper panel). Corresponding widths of the approximately Gaussian wavelength distributions for e and o polarization are $\Delta\lambda_{H1} \approx 8.3\,\text{nm}$ (FWHM) and $\Delta\lambda_{V1} \approx 10.1\,\text{nm}$ (FWHM), respectively. For spatial mode 2 (lower panel), we obtained $\overline{\lambda}_{H2} = 779.8\,\text{nm}$ and $\overline{\lambda}_{V2} = 779.4\,\text{nm}$ with corresponding width $\Delta\lambda_{H2} \approx 8.4\,\text{nm}$ (FWHM) and $\Delta\lambda_{V2} \approx 9.7\,\text{nm}$ (FWHM), respectively.

With the photons from the SMF sent directly into D1 and D2, bypassing the monochromators, a coincidence rate of $48000\,\mathrm{s}^{-1}$ is observed. The total coupling and detection efficiency extracted from the ratio of pair coincidences to single detector events on one side is 11 %.

The spectral distribution of the photons in each of the down-conversion modes individually for both the spatial modes defined by the SMF are characterized. We obtained wavelengths of $\overline{\lambda}_{H1} \approx 780.3\,\mathrm{nm}$ and $\overline{\lambda}_{V1} \approx 779.5\,\mathrm{nm}$ for spatial mode 1 (Fig. 3.2, upper panel). Corresponding widths of the approximately Gaussian wavelength distributions for e and o polarization are $\Delta\lambda_{H1} \approx 8.3\,\mathrm{nm}$ (FWHM) and $\Delta\lambda_{V1} \approx 10.1\,\mathrm{nm}$ (FWHM), respectively. For spatial mode 2 (Fig. 3.2, lower panel), we obtained $\overline{\lambda}_{H2} = 779.8\,\mathrm{nm}$ and $\overline{\lambda}_{V2} = 779.4\,\mathrm{nm}$ with corresponding width $\Delta\lambda_{H2} \approx 8.4\,\mathrm{nm}$ (FWHM) and $\Delta\lambda_{V2} \approx 9.7\,\mathrm{nm}$ (FWHM), respectively.

3.3 Wideband Polarization Correlations

In a first measurement, polarization correlations were evaluated without any spectral filtering of photon pairs coupled into the SMF (Fig. 3.3, upper panel), where we observe visibilities of $V_{\mathrm{HV}} = 94.8 \pm 0.2\,\%$ and $V_{45} = 68.4 \pm 0.3\,\%$, respectively*. With interference filters of 5 nm bandwidth (FWHM) centered at 780 nm, we observe visibilities of $V_{\mathrm{HV}} = 93.6 \pm 0.4\,\%$ and $V_{45} = 81.6 \pm 0.3\,\%$ (Fig. 3.3, lower panel).

After correcting for the four-photon contribution†, we obtain $V_{\mathrm{HV}} \in [97.9 \pm 0.3\%, 101.3 \pm 0.2\%]$ for measurements without a spectral filter, and $V_{\mathrm{HV}} \in [96.9 \pm 0.5\%, 99.7 \pm 0.5\%]$ with interference filters in place.

We conclude that the photon pair correlations due to the first-order down conversion process measured in the natural basis of the crystal (H/V) are close to 100 % and not affected by the spectral filtering, and that the reduced visibility V_{HV} in a direct measurement can be explained by higher-order down-conversion processes. This high visibility in the H/V basis for a large bandwidth will be an important component in our description of the polarization correlations later on when spectral degrees of freedom are included.

Using the same correction procedure for the polarization correlations in the com-

*Refer to Section 2.3.2 for details on the measurement procedure for V_{HV} and V_{45}.

†Refer to Section 2.3.3 for details on the correction procedure for the four-photon contribution.

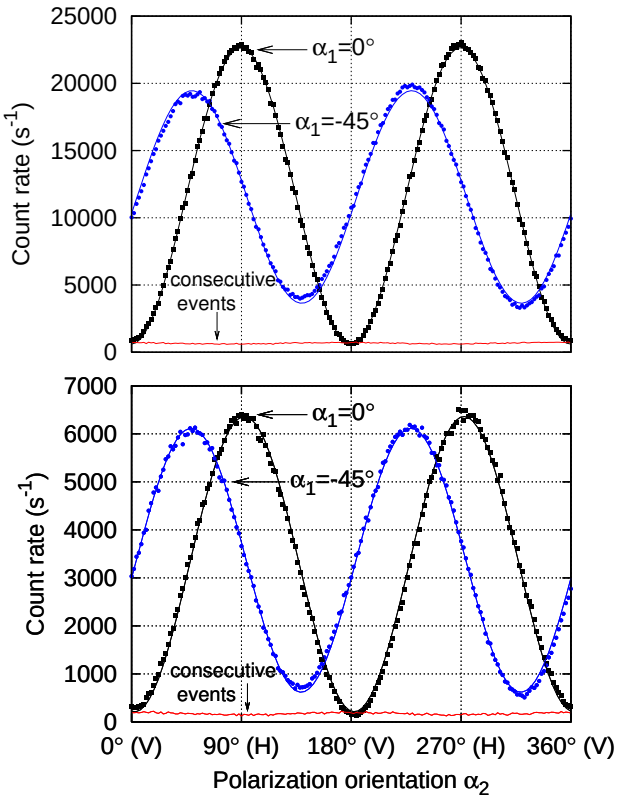

Figure 3.3: Polarization correlations measured in the H/V and $+45/-45°$ basis. The bottom trace in each panel represents pair coincidences from consecutive pulses. For the lower panel, 5 nm (FWHM) wide interference filters are inserted. Without spectral filters (upper panel), we observe direct visibilities of $V_{\mathrm{HV}} = 94.8 \pm 0.2\%$ and $V_{45} = 68.4 \pm 0.3\%$ without correcting for higher-order contributions; with spectral filters, the corresponding values are $V_{\mathrm{HV}} = 93.6 \pm 0.4\%$ and $V_{45} = 81.6 \pm 0.3\%$).

plementary basis, we obtain $V_{45} \in [69.1 \pm 0.3\%, 72.9 \pm 0.3\%]$ without spectral filters, and $V_{45} \in [83.1 \pm 0.3\%, 85.9 \pm 0.3\%]$ as confidence intervals due to the first-order down-conversion contribution. The lower visibilities in the complementary basis indicate a mixedness of the photon pair state in polarization space. Spectral filtering improves this visibility V_{45}, which will be characterized in more detail in Section 3.5.

3.4 Spectral Correlations

To investigate the relation between the spectral distribution and the polarization correlations, the monochromators M1, M2 were used in conjunction with the polarization analyzer. In the experimental runs, we fix the polarization analyzer orientations α_1, α_2 and record a two-dimensional map of coincidence events for a fixed integration time at each wavelength pair (λ_1, λ_2).

First, we consider the joint spectra of photon pairs for each of the two decay paths individually. Therefore, analyzers were fixed to the natural basis of the conversion crystal, selecting either H_1V_2 or V_1H_2 decays. The corresponding joint spectra acquired with a resolution of 0.5 nm are shown as density plots in Fig. 4.6. The integration time for each wavelength pair in this map was 22.5 s. For both polarization combinations, we observe approximately two-dimensional Gaussian distributions, which are almost aligned along one of the diagonals as suggested by the energy conservation for the down-conversion process. Contrary to a case with a narrow-band cw pump [96], the distribution is not restricted to a single line corresponding to a fixed energy sum $E_p = hc(\lambda_1^{-1} + \lambda_2^{-1})$. However, the covariance between the two wavelengths λ_1, λ_2 is not completely lost. This is mostly attributed to the larger bandwidth of the pump due to its short duration.

We further note that the two joint spectra for H_1V_2 and V_1H_2 coincidences in both collection modes are symmetric under exchange of λ_1 and λ_2, which simply reflects the fact that the two collection modes are chosen to exhibit a mirror symmetry with respect to a plane containing the optical axis of the crystal and the pump direction.

To quantify the spectral distributions, we use a two-dimensional Gaussian as a model:

$$g(\lambda_1, \lambda_2) \propto e^{-\frac{1}{2}\left[\frac{(\lambda_1-\bar{\lambda}_1)^2}{\sigma_1^2} + \frac{(\lambda_2-\bar{\lambda}_2)^2}{\sigma_2^2} + \frac{(\lambda_1-\bar{\lambda}_1)(\lambda_2-\bar{\lambda}_2)}{\sigma_{12}}\right]} \tag{3.4}$$

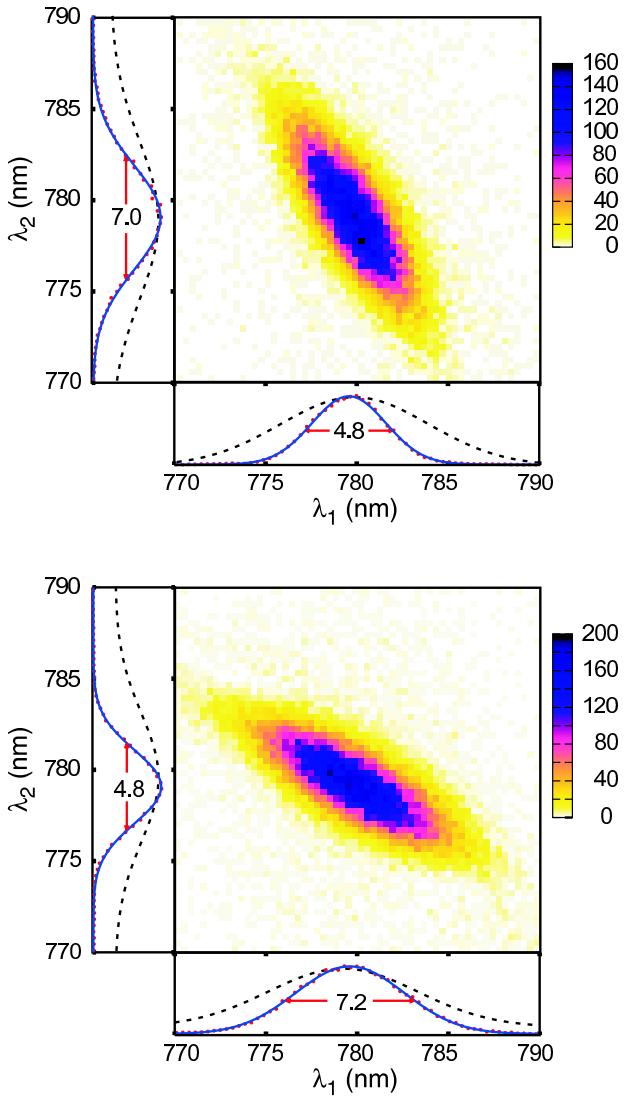

Figure 3.4: The joint spectra of coincidence counts for H_1V_2 polarizations (upper panel) and V_1H_2 (lower panel) polarization are different. Exchange of the λ_1 and λ_2 axis maps one onto the other. These joint spectra show the covariance between λ_1 and λ_2, which decreases with the broadening of the pump light. Different widths between the marginal (solid trace) and the single photon event spectrum (dotted trace), as well as differences between o and e polarization are apparent.

Therein, we obtain from a fit to the H_1V_2 joint spectrum displayed in the upper panel of Fig. 4.6 a central wavelength of $\overline{\lambda}_1 = 779.77 \pm 0.01\,\mathrm{nm}$ for the extraordinary, and $\overline{\lambda}_2 = 779.10 \pm 0.01\,\mathrm{nm}$ for the ordinary distribution, reflecting an alignment close to the degeneracy point. For the quantities governing the shape of the distribution, we obtain $\sigma_1 = 1.265 \pm 0.003\,\mathrm{nm}$, $\sigma_2 = 1.853 \pm 0.005\,\mathrm{nm}$ for the standard deviations, and $\sigma_{12} = 1.509 \pm 0.009\,\mathrm{nm}^2$ as a measure of the covariance of the two wavelengths.

Each distribution is *not* symmetric with respect to exchange in the two wavelengths. This will lead to spectral regions where the balance of the two decay paths necessary to observe a maximally entangled polarization state of the form Eq. 3.2 is not met. Another consequence of the asymmetry is a different width of the marginal distributions for both ordinary and extraordinary polarization. For the assumed two-dimensional Gaussian distribution, the marginals exhibit a width (FWHM) of

$$\Delta\lambda_{m1,2} = 2\sqrt{2\log 2}\left(\frac{1}{\sigma_{1,2}^2} - \frac{\sigma_{2,1}^2}{4\sigma_{12}^2}\right)^{-1/2} \tag{3.5}$$

or $\Delta\lambda_{m1} = 4.83 \pm 0.02\,\mathrm{nm}$ for the extraordinary polarization and $\Delta\lambda_{m2} = 6.97 \pm 0.05\,\mathrm{nm}$ for the ordinary polarization for the H_1V_2 combination and similar results for the V_1H_2 combination. Since the marginal distributions represent a conditional spectrum of having seen a photon at any wavelength in the other arm, this indicates that the collection bandwidth for both polarizations is slightly different due to the dispersion relations in the crystal for the phase matching conditions Eq. 3.1. In the SPDC process, the spectral distribution of down-converted photons is related to their angular dispersion. For a certain acceptance angle subtended by the collection, the e-polarized photons (which have a narrower spread in the emission direction) will be collected more efficiently than the o-polarized photon. Thus, not every photon detected in one spatial mode has its twin in the other mode [97]. This limits the overall collection efficiency of type-II SPDC for generating entangled photons.

Compared to the widths of the distributions of single photon events (dashed lines in the marginal distributions of Fig. 4.6, $\overline{\Delta\lambda_H} \approx 8.4\,\mathrm{nm}$, $\overline{\Delta\lambda_V} \approx 9.9\,\mathrm{nm}$*) the widths of the marginal spectra are also considerably smaller. This difference in spectral width [93] is an indicator for a reduced collection efficiency, in general in agreement with the reduced pair/single ratio observed in femtosecond-pumped SPDC sources.

*These values are obtained by averaging the width of the single photon spectrum from the two spatial modes for each respective polarization, i.e. $\overline{\Delta\lambda_H} = (\Delta\lambda_{H1} + \Delta\lambda_{H2})/2$.

To understand the effect of the spectral imbalance between the different polarization components on the polarization entanglement, we mapped out joint spectra for polarizations in a basis complementary to the natural polarizations of the crystal, or the ±45° linear polarizations in our case. The results are shown in Fig. 4.7, where the upper panel corresponds to polarization anti-correlations ($\alpha_1 = -\alpha_2 = 45°$), and the lower panel to polarization correlations ($\alpha_1 = \alpha_2 = 45°$). The integration time per wavelength pair was 30 s for the anti-correlations, and 60 s for the correlations. For the latter case, the mapping was done in a sequence of four interlaced grids. A drift of the system over the data acquisition period thus lead to a modulation of the coincidence counts at twice the final sampling spacing.

Since the phase δ between the two decay paths was adjusted to prepare photon pairs in a $|\Psi^-\rangle$ state, a relatively large overall count rate is observed for the polarization anti-correlations. As expected, a maximal coincidence count rate occurs at the degeneracy point and is progressively reduced away from it, following the spectral distribution of the overlap of the H_1V_2 and V_1H_2 contributions from Fig. 4.6. An interesting pattern is revealed for the anti-correlations: while there are no coincidences at the degenerate wavelength point, four regions with non-vanishing coincidence events are observed. These regions correspond to an imbalance in the decay path distribution, and will destroy the perfect polarization anti-correlations in the ±45° basis in an experiment where the wavelengths of both photons are ignored.

3.5 Spectrally Resolved Entanglement Characterization

The presence of residual polarization correlations at particular wavelength regions could be both due to the imbalance of both components, or due to a partially incoherent superposition between them as a consequence of entanglement with other degrees of freedom. We therefore carried out polarization correlation measurements on a larger set of relative analyzer angles for the different wavelength regions. Again we fixed the analyzer orientation for one mode to $\alpha_1 = +45°$, and varied the orientation for the other analyzer.

The result of (normalized) coincidence counts obtained during 60 s per polarizer setting for three representative regions in the spectral map are shown in Fig. 4.4. Trace A corresponds to a region with an excess of the $|V\rangle_1|H\rangle_2$ component, trace B to a region

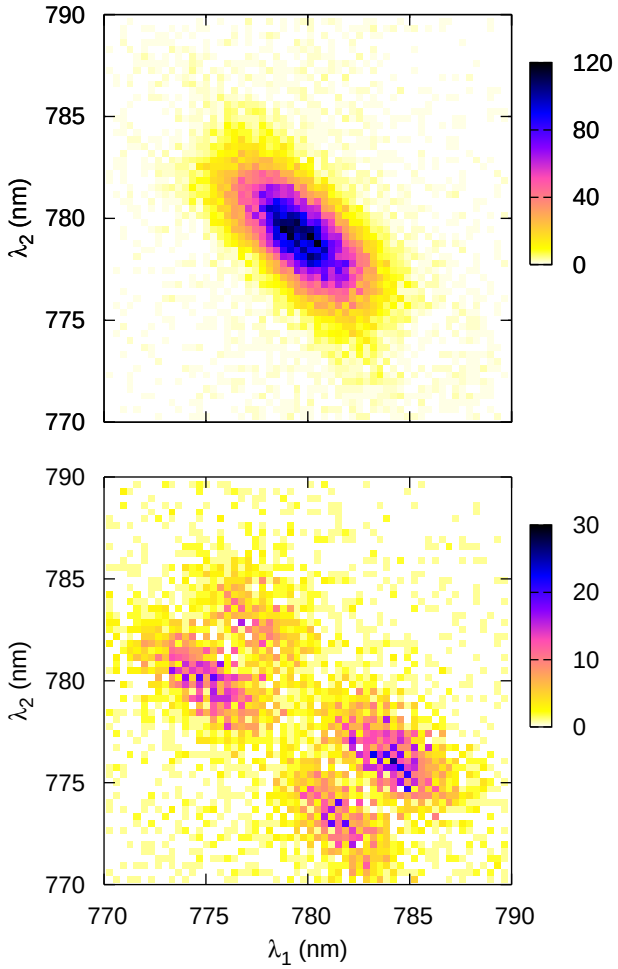

Figure 3.5: A joint spectrum of coincidences measured for a $+45°/-45°$ polarization combination (upper panel) reveals a pattern with the maximum coincidence rate at the degenerate wavelengths for a source adjusted to observe singlet Bell states $|\Psi^-\rangle$. The joint spectrum measured for a $+45°/+45°$ polarization combination (lower panel) exhibits four regions of higher count rate. These regions correspond to area with an imbalance of a and b. At the position of the degenerate wavelengths in the center, the coincidence rate is close to zero.

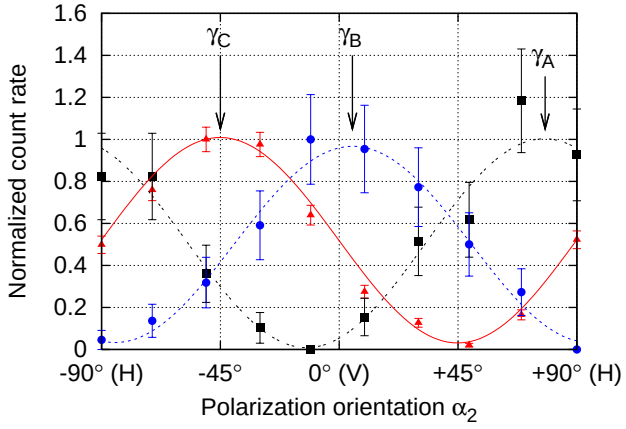

Figure 3.6: Polarization correlations at three different wavelength pairs where one photon is projected onto +45° polarization. The maximum of coincidences ranges from −45° polarization for a maximally entangled singlet Bell state (C), to the horizontal (A) or vertical (B) polarization.

with a predominance of the $|H\rangle_1|V\rangle_2$ contribution, and trace C to the degeneracy point. The normalization was carried out for better reading of the diagram due to the varying number of coincidences in the different spectral regions. It is apparent that at all points, the sinusoidal modulation of the polarization correlations shows a high visibility, while the angle α_2 for the maximum depends strongly on the spectral position. For the following, we denote this maximum angle by γ. For the three samples shown in Fig. 4.4, we obtained visibilities of $V_A = 98 \pm 12\%$, $V_B = 93 \pm 6\%$, and $V_C = 98 \pm 5\%$ from a sinusoidal fit, and rotations of $\gamma_A = 79.0 \pm 1.6°$, $\gamma_B = 5.0 \pm 0.8°$, and $\gamma_C = -45 \pm 0.6°$, respectively.

A map of both the visibility $V(\lambda_1, \lambda_2)$ and the angle $\gamma(\lambda_1, \lambda_2)$ for analyzer 1 at $\alpha_1 = +45°$ is displayed in Fig. 3.7 at wavelength pairs with a large enough coincidence count rate to extract visibilities with an uncertainty below 11%. This map confirms the high visibility of the polarization correlations for all wavelengths.

While quoting a high visibility V_{45} of polarization correlations with one of the polarizers oriented at 45° is in itself not enough to make a statement about the entanglement of photon pairs in general, the additional information that only two decay processes in SPDC are allowed reduces the discussion to an analysis of the coherence between

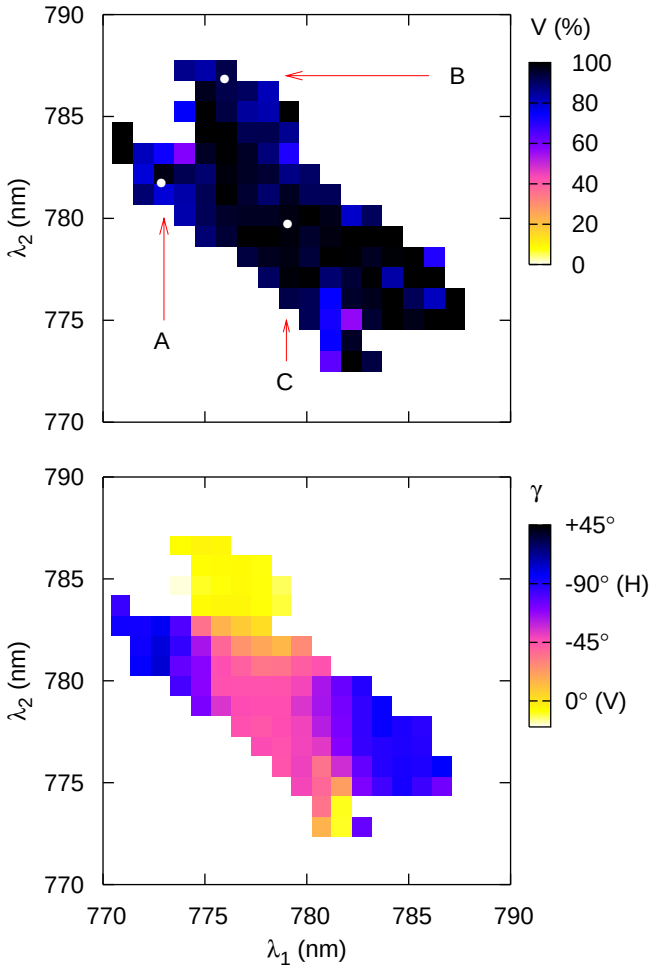

Figure 3.7: Map of the visibility V_{45} of polarization correlations for different sets of wavelengths (upper panel). We find a significant local increase compared to the global value obtained in figure 3.3. Points A, B and C correspond to the three detailed visibility measurements shown in Fig. 4.4. The lower panel indicates the angle γ for the maximal count rates, ranging from $-45°$ polarization for the singlet Bell state at (C) in the center towards horizontal polarization (A) for dominating $|V\rangle_1 |H\rangle_2$ contributions or vertical polarization (B) for prevailing $|H\rangle_1 |V\rangle_2$ contributions.

these decay processes. This is covered completely by the visibility measurement in the $+45°/-45°$ basis; hence its wide usage as a quick indicator for the entanglement quality of a photon pair source from SPDC.

These measurements, together with the fact that the first-order down-conversion process reveals also high visibility in H/V basis even without any spectral filtering (see Section 3.3), suggest that the superposition between two decay components is coherent, in accordance with assumptions in previous theoretical work [5]. The polarization state at each wavelength pair then can be written as:

$$|\Psi(\lambda_1, \lambda_2)\rangle = a\,|H\rangle_1|V\rangle_2 + b\,e^{i\delta}|V\rangle_1|H\rangle_2 \tag{3.6}$$

with two wavelength-dependent probability amplitudes $a(\lambda_1, \lambda_2)$ and $b(\lambda_1, \lambda_2)$. The fact that a high visibility is observed with linear polarizations at 45° suggests that there is no complex phase factor between the amplitudes a and b. For imbalanced amplitudes a and b the state is not maximally entangled anymore. The angle γ depends now only on the ratio between real-valued probability amplitudes a and b:

$$\gamma = -\arctan\frac{b}{a} \tag{3.7}$$

It is worth noting that the high symmetry of the imbalanced states in the frequency map allows for compensation techniques [1] that combine different spectral components so that they do not reveal information about the polarization. If this combination is performed appropriately, the spectral degree of freedom is factored out of the description of the state (much like the timing compensation performed by the compensation crystals) and no longer degrades the polarization entanglement.

Following the same model, we can use the spectral map of the $|H\rangle_1|V\rangle_2$ and $|V\rangle_1|H\rangle_2$ contributions displayed in Fig. 4.6 to extract a local measure for the entanglement quality in the polarization degrees of freedom: A commonly used quantity for this purpose is the entropy of entanglement S. For a local polarization state given by Eq. 3.6, the entanglement entropy is given by [83]

$$S(\lambda_1, \lambda_2) = -a^2\log_2(a^2) - b^2\log_2(b^2) \tag{3.8}$$

The spectral distribution of the probability amplitudes can be chosen as

$$\begin{aligned} a(\lambda_1, \lambda_2) &= \sqrt{\frac{g(\lambda_1, \lambda_2)}{g(\lambda_1, \lambda_2) + g(\lambda_2, \lambda_1)}} \\ b(\lambda_1, \lambda_2) &= \sqrt{1 - a(\lambda_1, \lambda_2)^2} \end{aligned} \tag{3.9}$$

with a spectral distribution $g(\lambda_1, \lambda_2)$ of photon pairs. Using a model expression according to Eq. 3.4 for g, we obtain an expected spectral entanglement entropy distribution shown in the upper panel of Fig. 3.8. Along the two diagonals, the entropy is maximal, indicating maximally entangled states due to the balanced contributions from both decay paths.

The lower panel of this figure shows the entanglement entropy S extracted from the distributions of both decay components obtained from measurements presented in Fig. 4.6. The entropy is only computed at locations where the overall count rate allowed for reasonable error bars. The distribution of maximally entangled states in the spectral map is clearly revealed.

3.6 Dependence of Entanglement Quality on Spectral Filtering

When the wavelengths of a photon pair are ignored and only polarization correlations are probed, integrating all spectral contributions with their varying γ results in a reduced overall visibility V_{45} even if the individual wavelength components exhibit a high visibility. In practice this results in a mixed state with lower entanglement quality; to remedy this, spectral filtering, either in the form of interference filters [7] or careful engineering of the collection bandwidth can be used [25]. These filters spectrally limit the λ_1, λ_2 of the down-converted photon pairs to a smaller region, thus reducing contributions with γ deviating from the value in the degeneracy point. Consequently, there is a tradeoff between the coincidence rate and the measured visibility. For very narrow spectral filters entanglement quality will be high but count rates low; as the filter bandwidth is increased, count rates increase but the entanglement quality is reduced. The polarization correlations underlying the visibility map, Fig. 3.7 (upper panel), offer a way to determine the optimal filtering scheme given some entanglement-based figure of merit.

For a virtual experiment with filter transmissions $f_{1,2}(\lambda_{1,2})$, the coincidence rate distribution $C(\alpha_2)$ necessary to determine the polarization correlation visibility for $\alpha_1 = 45°$ can be obtained by weighting the contributions $c(\lambda_1, \lambda_2, \alpha_2)$ from the different

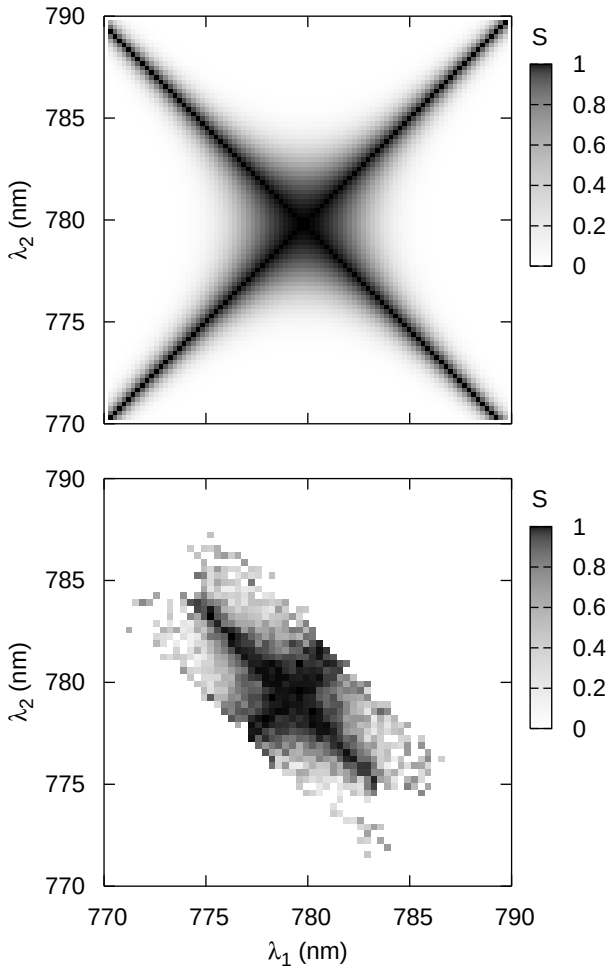

Figure 3.8: Entanglement quality. The upper panel illustrates the entanglement entropy S as a function of both wavelengths λ_1, λ_2 for a model distribution of non-overlapping contributions for $|H\rangle_1|V\rangle_2$ and $|V\rangle_1|H\rangle_2$ decay paths in SPDC according to Eq. 3.4. The lower panel shows $S(\lambda_1, \lambda_2)$ obtained from experimental polarization correlations in the $+45°/-45°$ basis of Fig. 4.6. The entanglement is maximal at positions with balanced contributions for both decay paths.

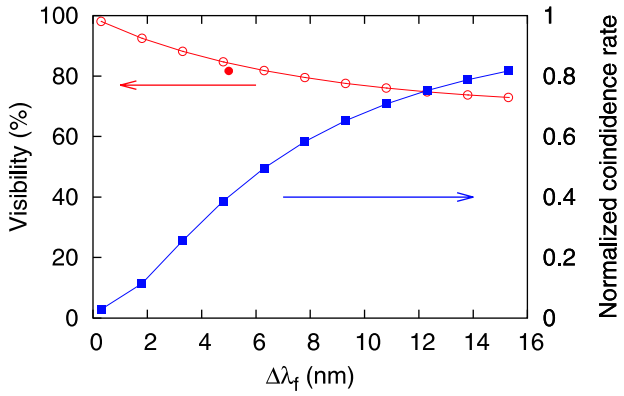

Figure 3.9: Visibility V_{45} (open circles) and normalized coincidence rates (filled squares) as a function of fixed filter bandwidth $\Delta\lambda_f$. The values were obtained by virtual filtering using the spectral map of visibility measurements leading to Fig. 3.7. The experimental point (filled circle) corresponds to a real filter with $\Delta\lambda_f = 5\,\text{nm}$, resulting in $V_{45} = 81.6\%$. Our result is consistent with predictions in [5].

wavelength pairs we already measured to generate the visibility map in Fig. 3.7:

$$C(\alpha_2) = \sum_{\lambda_1,\lambda_2} c(\lambda_1, \lambda_2, \alpha_2)\, f_1(\lambda_1) f_2(\lambda_2) \tag{3.10}$$

The visibility V_{45} itself is then extracted from a sinusoidal fit of $C(\alpha_2)$.

Typical filter transmission functions of narrow-band interference filters can be described by a Lorentzian profile and are characterized by their central wavelength $\overline{\lambda}_f$ and bandwidth $\Delta\lambda_f$ (FWHM). The resulting integral visibility V_{45} for filters with the same transmission profiles $f_1(\lambda) = f_2(\lambda)$ centered at the degeneracy wavelength in both arms is shown in Fig. 3.9 (open circles). As expected, the visibility drops with an increasing bandwidth $\Delta\lambda_f$ of the filters, in agreement with the theoretical predictions in [5]. We also include a normalized coincidence count rate (filled squares) extracted out of the weighted virtual counts $C(\alpha)$ to illustrate the loss of pairs at narrow bandwidths.

As a check of consistency, we can compare the expected visibility from virtual filtering with a direct measurement of the V_{45} for a filter with $\Delta\lambda_f = 5\,\text{nm}$. From Fig. 3.9 we expect $V_{45} = 84.5\%$, in agreement with the observed confidence interval for $\tilde{V}_{45}$ in Section 3.2 for the first order down-conversion process after correction for higher-order contributions.

Chapter 4

Elimination of Spectral Distinguishability in Ultrafast SPDC

For experiments which require photon pairs to exhibit tight localization in time [8, 74], or for preparation of entangled states between more than two photons [62, 64, 77], the SPDC process needs to be pumped by ultrafast optical pulses. Such sources often exhibit a reduction in the quality of polarization entanglement arising from spectral distinguishability of the possible decay paths. This has been addressed theoretically [5, 88, 98]; more recently, experiments investigating the underlying phenomenon have been performed [93, 94, 95, 97, 99]. Various techniques are implemented to eliminate spectral distinguishability: they range from specific tailoring of the down-conversion medium [90, 91], double-pass configuration of the pump beam [92] to interferometric setups [89].

In the previous experiment, we have shown that the wider spectral distribution of ordinarily (o) polarized down-converted light in comparison with the extraordinary (e) component translates into a spectral distinguishability between the two decay paths for type-II SPDC [97]. When only the polarization degree of freedom is considered, this spectral distinguishability reduces the purity of a state and thus the entanglement quality. Typically, strong spectral filtering is applied in order to detect only photons

which fall into the non-distinguishable part of the spectrum. However, any form of spectral filtering drastically reduces the count rate. This is especially disadvantageous in multi-photon experiments where the coincidence rate decreases rapidly with any filter loss. A scheme that can eliminate the spectral distinguishability without significant loss of signal will benefit these experiments greatly. One of the ways to overcome this problem is the spectral compensation scheme proposed and first implemented by Kim *et al.* [1]. In this chapter I will present a detailed experimental study of the effectiveness of this method.

4.1 Spectral Compensation with Two-Photon Interference

In the "classic" method of generating polarization-entangled photon pairs in non-collinear type-II parametric down conversion, photon pairs are collected at the intersection of the e and o-polarized emission cones [7]. Their combined state covering polarization, direction, and spectral fingerprint can be written as

$$|\Psi\rangle = \frac{1}{\sqrt{2}}\left(|H_e\rangle_1|V_o\rangle_2 + e^{i\delta}|V_o\rangle_1|H_e\rangle_2\right), \tag{4.1}$$

where δ is the free phase between the states $|H_e\rangle_1|V_o\rangle_2$ and $|V_o\rangle_1|H_e\rangle_2$ corresponding to the two conversion paths.

In the spectral compensation scheme (Fig. 4.1), a half-wave plate ($\lambda/2$) placed in one of the arm rotates the polarization by 90°, such that both photons arrive at the polarization beam splitter (PBS) with the same polarization. The $|H_e\rangle_1|V_o\rangle_2$ combination is transformed into $|V_e\rangle_1|V_o\rangle_2$, so both photons are reflected by the PBS (RR path), while the $|V_o\rangle_1|H_e\rangle_2$ combination is transformed into $|H_e\rangle_1|H_o\rangle_2$, so both photons are transmitted by the PBS (TT path). Regardless of their polarization state, photons carrying the spectral fingerprint of o and e polarization from the original conversion process will always emerge at a corresponding port of the PBS. As long as there is no path difference between the down conversion crystal and the PBS, neither the arrival time nor the spectrum of the photon will reveal information of the input polarization state, decoupling the temporal and spectral degree of freedom from the polarization. The o and e-polarized photons need not arrive strictly simultaneously at the PBS for the scheme to work, as shown in various two-photon interference experiments [100, 101]. Similarly to the Hong-Ou-Mandel interference of photon pairs [102], this scheme does

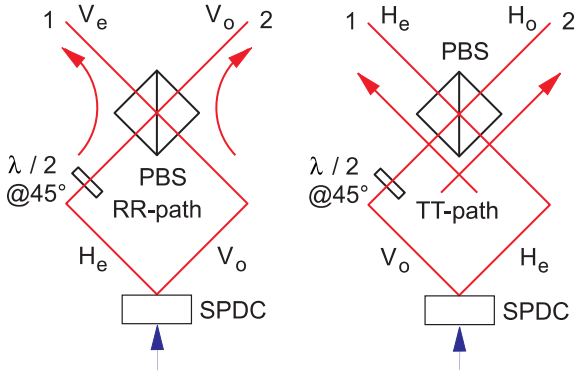

Figure 4.1: The possible paths of the photon pair generated in spontaneous parametric down conversion (SPDC) for the two corresponding down-converted components. The e and o-polarized photons will exit at the different ports of the PBS independent of their polarization.

not require path length stability to a fraction of the wavelength, but only to a fraction of the coherence length of the photons. It is also simple in the sense that it requires no special engineering of the down-conversion medium or complex double-pass setups. For a free phase $\delta = \pi$, the photon pairs are in the Bell state

$$|\Phi^-\rangle = \frac{1}{\sqrt{2}} \left(|H\rangle_1 |H\rangle_2 - |V\rangle_1 |V\rangle_2 \right) , \tag{4.2}$$

which we will investigate for the rest of the chapter.

4.2 Experimental Setup

Like in the previous experimental setup, we have implemented a polarization-entangled photon pair source using type-II phase matching in a crossed-ring configuration [7] and use polarization filters and grating monochromators to resolve the different spectral components for both photons (Fig. 5.2). As this source is primarily geared towards the generation of polarization-entangled four-photon state, we have switched the Ti:Sapphire (Ti:Sa) laser in the previous experiment to one that is capable of a higher output power*. The focus of the blue pump at the down-conversion crystal has also

*For this experimental setup, we are using a Tsunami (Spectra-Physics) Ti:Sa laser pumped by 10 W of 532 nm light from a Millennia Pro (Spectra-Physics) solid-state pump laser.

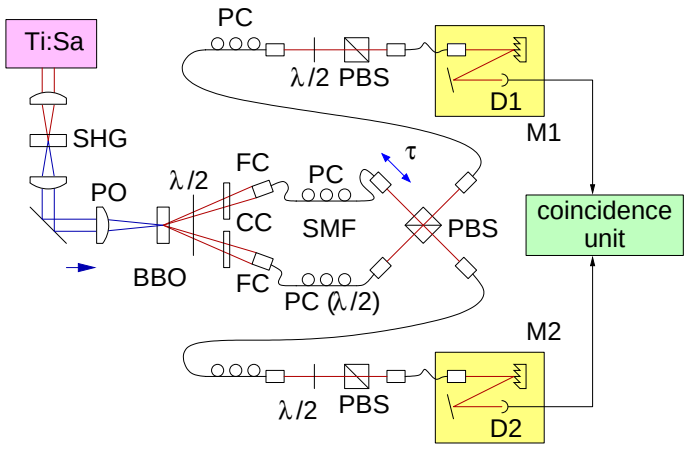

Figure 4.2: Experimental setup. Photon pairs generated via SPDC in a nonlinear crystal (BBO) pumped by femtosecond optical pulses are collected into single-mode optical fibers (SMF). A half-wave plate ($\lambda/2$) and polarizing beam splitter (PBS) combination renders them spectrally indistinguishable. The down-converted photons then pass through polarization filters and subsequent grating monochromators for analysis.

been reduced in an attempt to get a higher four-photon production rate.

4.3 Wideband Polarization Correlations

To probe the quality of polarization entanglement between the photon pairs, polarization correlations in the H/V basis (the natural basis, i.e., the basis aligned to the crystal axes) and $+45/-45°$ basis (the complementary basis) are measured. In the H/V basis, we expect to see nearly perfect correlations due to the type-II conversion process. In the $+45/-45°$ basis, the level of (anti-)correlation will depend on the degree of indistinguishability between the two decay paths. For $|\Phi^-\rangle$, perfect anti-correlation in the $+45/-45°$ basis is expected, but residual distinguishability of the decay paths will deteriorate this.

To assess the degree of distinguishability, coincidences between the detectors over a range of delays τ are recorded for $\alpha_1 = -\alpha_2 = +45°$. The result is shown in Fig. 4.3, which reveals clearly a bump for $\tau = 0$. A fit to a Gaussian distribution reveals a FWHM of approximately 100 fs, corresponding to the coherence time of the down-

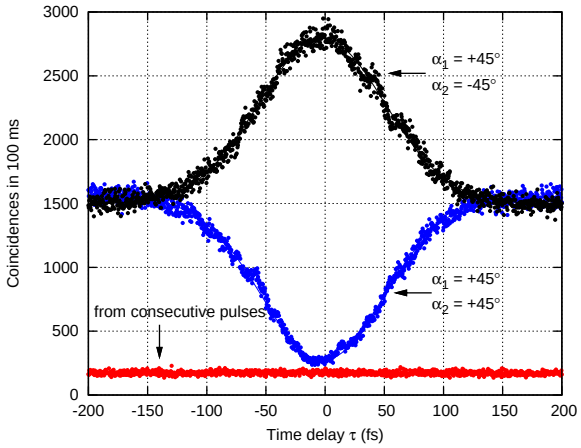

Figure 4.3: Polarization correlations measured in the $+45°/-45°$ basis as a function of delay τ. Polarization analyzers were oriented at $\alpha_1 = -\alpha_2 = +45°$ for the bump and at $\alpha_1 = \alpha_2 = +45°$ for the dip. The bottom trace represents pair coincidences from consecutive pulses. Without correcting for higher-order contribution, the visibility of the dip is $85 \pm 2\,\%$. The band of confidence for the corrected value is $[90 \pm 2\%, 96 \pm 3\%]$. Refer to the Section 2.3.3 for details on the correction procedure.

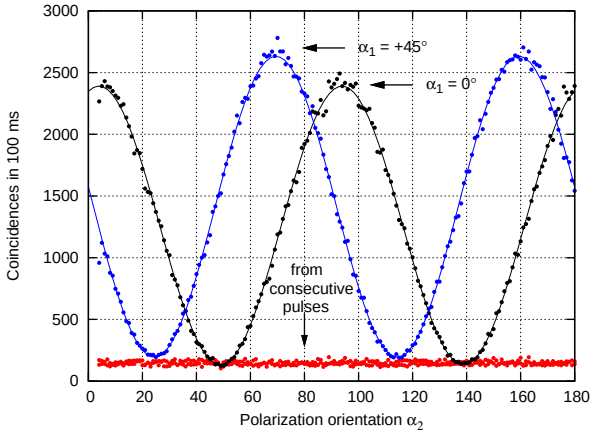

Figure 4.4: Polarization correlations in the H/V and $+45°/-45°$ bases. The bottom trace represents pair coincidences from consecutive pulses. Without correcting for any higher-order contribution, we observed direct visibilities of $V_{HV} = 90.0 \pm 0.4\%$ and $V_{45} = 86.8 \pm 0.4\%$.

converted photons. By choosing $\alpha_1 = \alpha_2 = +45°$, a corresponding dip in coincidences is observed. From Fig. 4.3, the maximal visibility of the dip is $85 \pm 2\,\%$.

The polarization entanglement of the photon pairs was characterized by measuring the visibilities V_{HV} and V_{45}*. Without spectral filtering, we obtain results $V_{HV} = 90.0 \pm 0.4\%$ and $V_{45} = 86.8 \pm 0.4\%$ (see Fig. 4.4). After correcting for the four-photon contribution†, we obtain bands of confidence for the visibilities, $V_{HV} \in [95.1 \pm 0.5\%, 100.8 \pm 0.5\%]$ and $V_{45} \in [92.0 \pm 0.4\%, 97.9 \pm 0.5\%]$ for the process leading to pairs only.

Both the bounds for V_{45} are significantly higher than the results obtained in the previous experiment [97] where the spectral compensation is not implemented. There we see $V_{45} \in [69.1 \pm 0.3\%, 72.9 \pm 0.3\%]$ without spectral filtering, and $V_{45} \in [83.1 \pm 0.3\%, 85.9 \pm 0.3\%]$ with spectral filtering. This shows that the spectral compensation scheme has eliminated the distinguishability between the two down-converted components.

To provide a consistency check for the correction procedure, measurements of the visibilities are made with various pump powers. A model describing the dependence of

*Refer to Section 2.3.2 for details on the measurement procedure for V_{HV} and V_{45}.

†Refer to Section 2.3.3 for details on the correction procedure for the four-photon contribution.

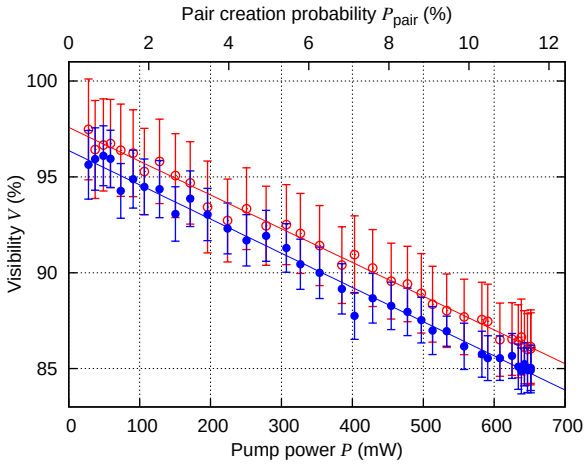

Figure 4.5: Visibility V_{HV} (open circles) and V_{45} (solid circles) measured as a function of the pump power. The probability of creating a pair P_{pair} (top axis) is proportional to the pump power. Solid lines show linear fits to the visibility reduction. From the slope, a pair generation probability can be derived via Eq. 4.5 (top axis). At low power, the coincidences are dominated by the contribution from first order down-conversion. The extrapolated visibilities at $P = 0$ $V_{HV} = 97.6 \pm 0.1\%$ and $V_{45} = 96.4 \pm 0.1\%$.

visibility on pump power is described in [23]. It assumes that the detected pair rate has a contribution R_2 from pairs generated in the same birth process, and a contribution R_4 from partially detected, incoherent double pair events. They can be written as

$$\begin{aligned} R_2 &= P_{\text{pair}} \frac{1+\cos\theta}{2}, \\ R_4 &= 4\, P_{\text{double pair}} \frac{2+\cos\theta}{4}, \end{aligned} \tag{4.3}$$

where $\theta = \alpha_1 - \alpha_2$, and P_{pair} and $P_{\text{double pair}}$ are the probabilities for creating a pair and an incoherent double pair per pulse, respectively. The first one can be written as

$$P_{\text{pair}} = \frac{S}{\eta_c \eta_q f}, \tag{4.4}$$

where S is the rate of detector events on one side, η_c characterizes the coupling efficiency, η_q is the quantum efficiency of the detectors, and f the repetition rate of the laser. Assuming a Poissonian distribution in the counting of incoherent pairs events, one finds $P_{\text{double pair}} = P_{\text{pair}}^2/2$. The visibility V obtained from the sum of R_2 and R_4 is

$$V \approx V_{\max} - P_{\text{pair}}, \tag{4.5}$$

with $V_{\max}$ being the limit for the visibility at low pump power. Figure 4.5 shows the visibilities observed for different pump powers, exhibiting a linear decrease with power as expected according to Eq. 4.5. The slope of both visibility measurements coincide ($0.0177 \pm 0.0003\%\,\text{mW}^{-1}$) and allows to rescale power into pair probability (see top axis on figure). From the pair probability and a single detector event rate (corrected for saturation effects), a combined detector/coupling efficiency of 11.3% can be derived via Eq. (4.4).

The limit $V_{\max}$ for the visibility at low pump power are $V_{HV} = 97.6 \pm 0.1\%$ and $V_{45} = 96.4 \pm 0.1\%$ in agreement with results from the correction procedure.

4.4 Spectral Correlations

Like in the previous experiment, to understand the joint spectral properties of the polarization correlations, we measured the joint spectrum of the photon pairs generated from each of the two decay paths. As the source is producing photon pairs with an approximate $|\Phi^-\rangle$ polarization state (Eq. 5.4), this is done by fixing the polarization

analyzers to the natural basis of the down-conversion crystal, selecting either the H_1H_2 or V_1V_2 decay path. The spectra are taken with a resolution of 0.5 nm and an integration time of 30 s for each wavelength pair.

Our results (shown in Fig. 4.6) have nearly identical distributions, with the exception of their maximum coincidence rate. A balanced contribution between the H_1H_2 and V_1V_2 decay path is found at all wavelength pairs, compatible with state $|\Phi^-\rangle$ at every point. This is in contrast with results obtained without spectral compensation [97] shown in the previous chapter, with the different spectral fingerprints of the two decay paths.

The marginal distributions λ_1, λ_2 exhibit widths of $\Delta\lambda_{m1} = 9.2 \pm 0.3$ nm (FWHM) and $\Delta\lambda_{m2} = 5.8 \pm 0.2$ nm (FWHM) for the H_1H_2 combination. A comparable distribution is also observed for the V_1V_2 joint spectrum (Fig. 4.6, lower panel). Thus, the spectral degree of freedom no longer reveals any information on the corresponding polarization state. The spectral distribution of the photons collected in each spatial mode obtained from the same run have a FWHM of $\overline{\Delta\lambda_1} \approx 10.5$ nm and $\overline{\Delta\lambda_2} \approx 8.3$ nm*) The wider spectral distribution corresponds to the distribution of the o-polarized photons while the narrower spectral distribution corresponds to the e-polarized photons. We note that the single photon spectral distributions (dashed lines in Fig. 4.6) are wider than the marginals, $\Delta\lambda_{m1} = 9.2$ nm, $\Delta\lambda_{m2} = 5.8$ nm. This disparity, also observed in the previous experiment, is caused similarly by the difference in the width of the spectral distribution between the e and o-polarized photon [97].

The joint spectra for polarizations in the complementary basis, $(+45°/+45°)$, are shown in Fig. 4.7, normalized to the total events both in the $+45°/+45°$ and $+45°/-45°$ basis. For comparison, the upper panel shows the result without spectral compensation [97] obtained in the previous experiment. It reveals regions with higher rates, indicating an imbalance between the two down-converted components in those areas. With the spectral compensation (lower panel), the distribution of uncorrelated pair events is compatible with the four-photon contribution. This can be seen from the marginal distribution of the joint spectrum, $\Delta\lambda_{m1} = 10.8 \pm 0.4$ nm, $\Delta\lambda_{m2} = 8.4 \pm 0.2$ nm (FWHM) which is identical to the distribution of the photon collected in each spatial mode.

To characterize the distinguishability between the two decay paths, we also need to

*These values are obtained by averaging the width of the single photon spectrum from the two spatial modes for each respective polarization, i.e. $\overline{\Delta\lambda_1} = (\Delta\lambda_{H1} + \Delta\lambda_{V1})/2$.

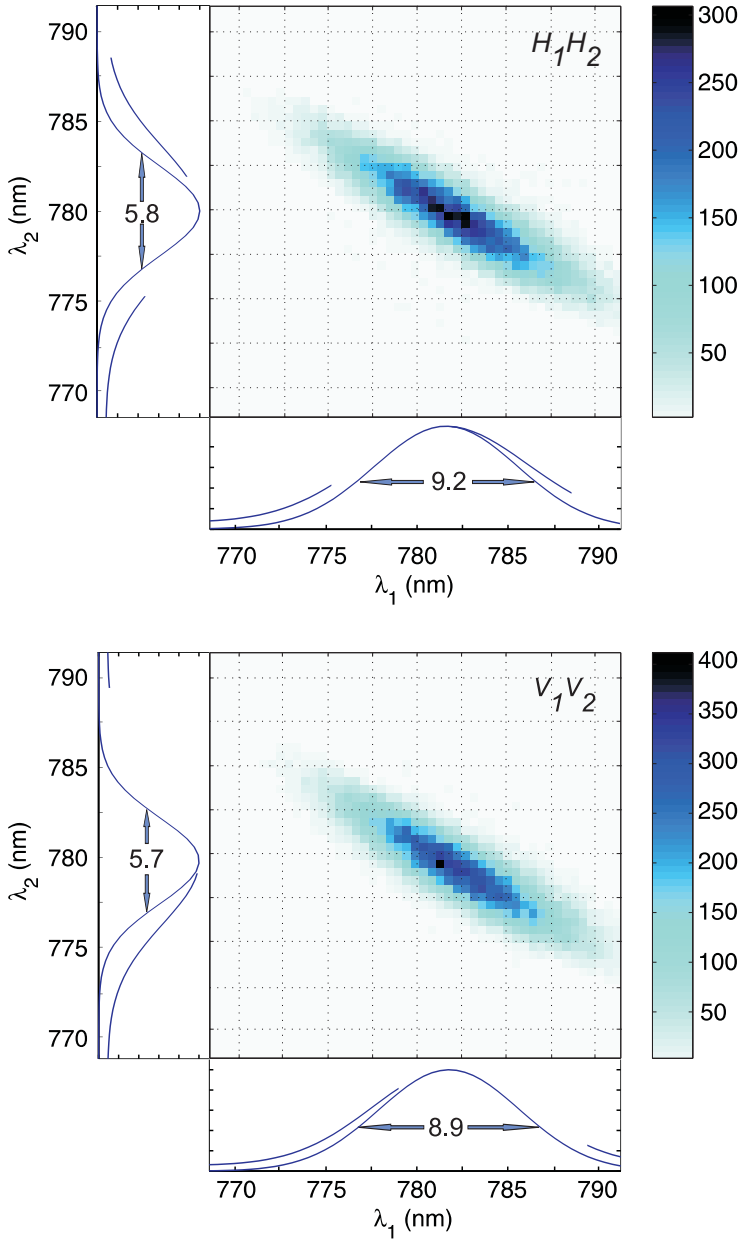

Figure 4.6: Joint spectra of coincidence counts in 30 s for H_1H_2 (upper panel) and V_1V_2 (lower panel) polarizations. The spectra corresponding to the two decay paths RR and TT are almost identical with the exception of the difference in the maximum count rate recorded. Differences between the widths of the marginal (solid trace) and the single photon spectra (dashed traces), as well as between the e and o polarization are observed as expected.

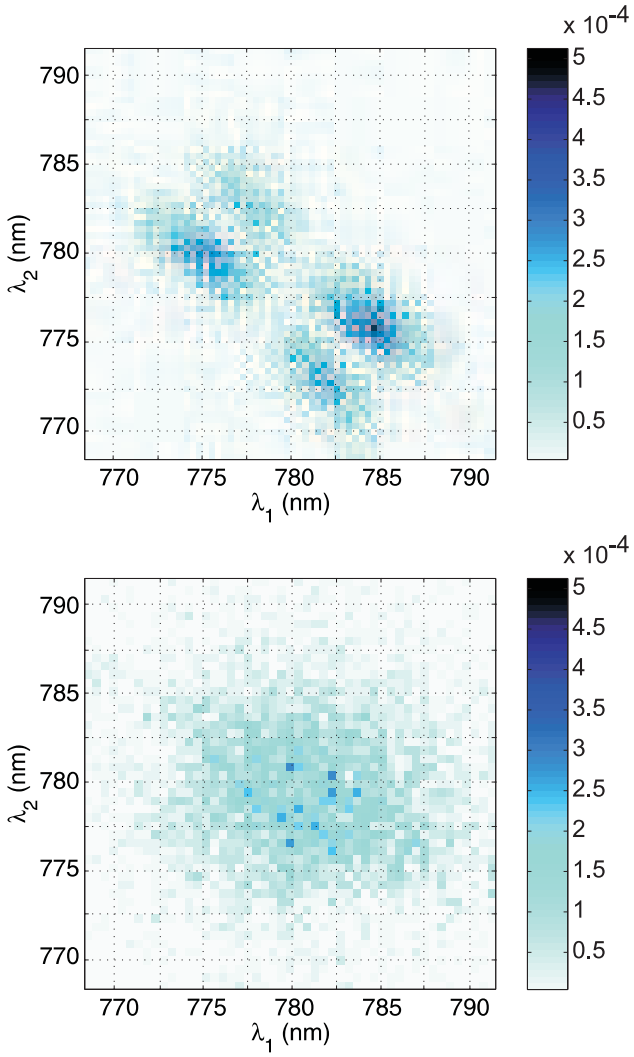

Figure 4.7: Joint spectra of coincidences measured for the +45°/+45° polarization combination. The counts are normalized to the total events in the spectral mapping experiments for both configurations. Without the spectral compensation scheme (upper panel), the joint spectrum exhibits four regions of higher count rate, comprising a fraction of 0.14 of all events. They correspond to areas with an imbalance of the two decay paths. With the spectral compensation scheme (lower panel), the joint spectrum, a fraction of 0.10 of the total events, exhibits a distribution of uncorrelated pair events about the degenerate wavelength which is compatible with estimates of the four-photon contribution.

look at the corresponding $+45°/-45°$ joint spectrum. Together with this measurement, the visibility V_{45} can be reconstructed by summing over all wavelengths:

$$V_{45} = \frac{\sum\limits_{\lambda_1,\lambda_2} c^{+,-}(\lambda_1,\lambda_2) - \sum\limits_{\lambda_1,\lambda_2} c^{+,+}(\lambda_1,\lambda_2)}{\sum\limits_{\lambda_1,\lambda_2} c^{+,-}(\lambda_1,\lambda_2) + \sum\limits_{\lambda_1,\lambda_2} c^{+,+}(\lambda_1,\lambda_2)}\,, \tag{4.6}$$

where the $c^{+,\pm}(\lambda_1,\lambda_2)$ are coincidence events detected for various wavelength pairs, and $+-$ and $++$ refers to the $+45°/-45°$ and $+45°/+45°$ polarizer settings.

After correcting for the four-photon contribution, we get $V_{45} \in [73.8 \pm 0.5\%, 80.2 \pm 0.6\%]$ without spectral compensation. With spectral compensation, we get $V_{45} \in [89.4 \pm 0.5\%, 100.4 \pm 0.6\%]$.

Chapter 5

Violation of Spin-1 CHSH Inequality

The term "quantum entanglement" describes the non-classical correlations that exist between the component entities of certain composite quantum systems. Due to the presence of these non-classical correlations, a full quantum mechanical description of such a composite system is no longer possible just by appealing to the descriptions of the components in isolation. A complete description of such a quantum system is only possible when it is considered in its entirety.

An example of such a composite system is described in the EPR-Bohm (EPRB) thought experiment [32]. The bipartite system (Fig. 5.1) consists of a source of spin-$\frac{1}{2}$ (two-level) particles, i.e. electron and positron from the decay of a neutral π meson

$$\pi^0 \rightarrow e^- + e^+. \tag{5.1}$$

As the pion has zero spin, by conservation of angular momentum, the spin state of the system can be written as a singlet configuration described by

$$|\Psi^-\rangle = \frac{1}{\sqrt{2}} \left(|\uparrow_{e^-}\downarrow_{e^+}\rangle - |\downarrow_{e^-}\uparrow_{e^+}\rangle \right). \tag{5.2}$$

This is called an entangled state and is not expressible as a product of the individual spin state of the electron and positron. For the same reason, the state is said to be nonseparable.

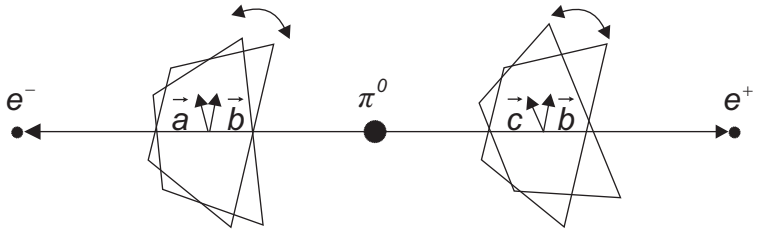

Figure 5.1: The EPR-Bohm thought experiment. In the experiment, the decay of a neutral π meson act as a source of electron and positron. As the pion has zero spin, by conservation of angular momentum, the spin state of the system can be written as a singlet configuration described by Eq. 5.2. Spin measurement of either the electron or positron in any arbitrary direction $\vec{a}$, $\vec{b}$, or $\vec{c}$ will have equal probability of yielding spin-up and spin-down. However, when comparing the results of the spin of both particles measured in the same direction, they show perfect anti-correlation.

The quantum correlations between the particles in the various composite quantum systems lend themselves to the basic requirements for certain quantum computation [60, 61, 62, 63] and communication [39] protocols. The performances of these protocols are strongly dependent on the quality of entanglement between the particles in the system or the fidelity of the entangled state in the experimental implementation in comparison to that described in an idealized model of the system. There are a number of measures for entanglement quality [83, 84] and fidelity [103, 104] of entangled quantum states. These measures often require a full characterization of the quantum state of the system being investigated to establish those quantities. However, if the objective is just to detect the presence of entanglement in a system or to provide a loose comparison of the entanglement quality between quantum states, a simpler measure will be an entanglement witness.

Entanglement witnesses are a class of functions that allows us to distinguish an entangled state from a separable one. A well known example of such a function is Bell inequality* [33]. It was derived by John S. Bell in 1987 to address the question of whether the quantum mechanical description of nature is complete or that the seemingly nonlocal effects associated with composite quantum systems are actually mediated by

*The term Bell inequality is now commonly used as a generic name for all the entanglement witnesses that are formulated in the form of an inequality.

some local hidden variables (LHV). Since these local hidden variables are classical in nature, the Bell inequality is formulated in such a way that it sets an upper bound for classical correlations. Quantum correlations which are stronger will lead to the violation of this upper bound. The original form of the Bell inequality is written as

$$|P(\vec{a},\vec{b}) - P(\vec{a},\vec{c})| \leq 1 + P(\vec{b},\vec{c}), \tag{5.3}$$

where $\vec{a}$, $\vec{b}$, and $\vec{c}$ are the direction of the spin measurements shown in Fig. 5.1. The term $P(\vec{a},\vec{b})$ is the average value product of the spins measured in direction $\vec{a}$ and $\vec{b}$, respectively. This inequality will be violated for certain systems when there is (quantum) entanglement between the component particles. It should be noted that if the noise within a system is above a certain level, the system will not violate the Bell inequality even though there is entanglement between the component particles.

In 1969 the original Bell inequality is rederived by John F. Clauser, Micheal A. Horne, Abner Shimony, and Richard A. Holt into a form that includes an experimentally determinable parameter S. This rederived form came to be known as the CHSH inequality [34]. Another improvement of the CHSH inequality over the original Bell inequality is that it is no longer restricted to experiments where measurements only have two possible outcomes. This makes it possible to generalize the CHSH inequality to higher-dimensional bipartite systems. For the rest of this chapter, I will be presenting just such a generalization to higher dimension by experimentally violating the spin-1 (three-level) CHSH inequality with photons from the polarization-entangled four-photon source implemented in the previous experiment to demonstrate the presence of entanglement in the system.

5.1 Experimental Setup

The source of polarization-entangled photons (Fig. 5.2) using type-II phase matching in a crossed-ring configuration [7] that we implemented in the previous experiment*, is used for the measurements presented in this chapter. In the setup, the photon pairs collected after the spectral compensation are in the Bell state

$$|\Phi^-\rangle = \frac{1}{\sqrt{2}}\left(|H\rangle_1|H\rangle_2 - |V\rangle_1|V\rangle_2\right) . \tag{5.4}$$

*Refer to Section 4.2 for details on the setup used for the generation of polarization-entangled photons in this experiment.

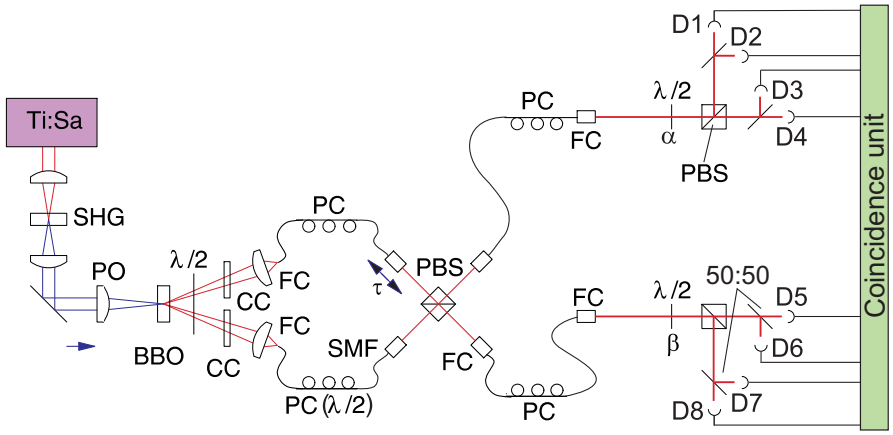

Figure 5.2: Experimental setup. The source of polarization-entangled photons implemented in the previous experiment is used for the measurements presented in this chapter. Non-polarizing beam splitters with a splitting ratio of 50:50 are placed behind each of the two output ports of both polarizing beam splitters (PBS). This allows for the probabilistic splitting of two photons in each spatial mode defined by the single mode optical fibers (SMF) in 50 % of the cases. Outputs of the eight detectors (D1 to D8) are sent into a coincidence unit where they are recorded and analyzed for all possible patterns of coincidences within a time window shorter than the repetition period of the pump laser.

The state of the double photon pairs produced by the second-order down-conversion process*, assuming coherence between the pairs, can be written as

$$|\Phi^-\rangle^{(2)}_{polarisation} = \frac{1}{\sqrt{3}}(|HH\rangle_1|HH\rangle_2 - |HV\rangle_1|HV\rangle_2 + |VV\rangle_1|VV\rangle_2). \tag{5.5}$$

Now two photons are found in each spatial mode defined by the single mode optical fiber (SMF). It should be noted in such bipartite configuration, the state $|HV\rangle$ and $|VH\rangle$ exist in a single spatial mode and are thus not distinguishable. In the analyzers, after passing through the polarizing beam splitter (PBS), the two photons in the $|HV\rangle$ combination always end up in different output ports. However, to detect the $|HH\rangle$ and $|VV\rangle$ combinations, modifications on the polarization analyzers are required. Non-polarizing beam splitters with a splitting ratio of 50:50 are placed behind each of the two output ports of both PBS. This allows for the probabilistic splitting of two photons in each spatial mode. Statistically, the two photons in the $|HH\rangle$ and $|VV\rangle$ combinations

*Refer to Section 2.1.2 for explanation on the process of second-order down-conversion.

will only end up in different ports of the 50:50 half of the time. For this reason, any measurements involving the detection of the $|HH\rangle$ and $|VV\rangle$ combinations will need to be multiplied by a factor of 1/0.5, e.g. the $|HH\rangle_1|HH\rangle_2$ events need to be multiplied by a factor of $1/(0.5)(0.5)$.

Outputs of the eight detectors (D1 to D8) are sent into a coincidence unit where they are recorded and analyzed for all possible patterns of coincidences within a time window shorter than the repetition period of the pump laser. The count rate for two-fold to eight-fold coincidence events (sum over all possible polarization combinations) are summarized in Table 5.1. Also included in the table for comparison are the count rates normalized to the two-fold events. From the previous experiment, we got a two-fold coincidence rate of $\approx 100000\,\mathrm{s}^{-1}$. With the current analyzer setup, we recorded a four-fold coincidence rate of $\approx 40\,\mathrm{s}^{-1}$. It is also possible to see that the six-fold and eight-fold coincidence rates are negligible. Thus, the four-fold coincidences do not need to be corrected for higher-order contributions.

Table 5.1: Comparison Between Different Order of Coincidences

Order of Coincidence	Count Rate (s^{-1})	Normalized Count Rate (%)
2	≈ 100000	100
4	≈ 40	≈ 0.04
6	≈ 0.005	≈ 0
8	0	0

5.2 Derivation of the Spin-1 CHSH Inequality

By defining the outcome $|HH\rangle$, $|HV\rangle$, and $|VV\rangle$ as $|1\rangle$, $|0\rangle$, and $|-1\rangle$ state, respectively, the state $|\Phi^-\rangle^{(2)}_{polarization}$ can be rewritten. This rewritten state, which we will denote simply as $|\Phi^-\rangle^{(2)}$, is given by

$$|\Phi^-\rangle^{(2)} = \frac{1}{\sqrt{3}}\left(|1\rangle_1|1\rangle_2 - |0\rangle_1|0\rangle_2 + |-1\rangle_1|-1\rangle_2\right). \tag{5.6}$$

The state $|\Phi^-\rangle^{(2)}$ now describes a system that is fully equivalent to a bipartite system consisting of entangled spin-1 particles. It is important to note that the term spin-1

used here refers to the two-photon polarization-entangled state and not the spins of photons themselves.

Thus, following closely the steps for the derivation of the spin-1 CHSH inequality presented in [105], we start by considering a bipartite system consisting of entangled spin-1 particles. Conventionally, the two modes of the system are called Alice and Bob, respectively. As in the case of the original Bell inequality [33], the derivation of the CHSH inequality [34] is based on two fundamental assumptions. They are

1. Correlations between result of measurements made by Alice and Bob can be accounted by a local realistic theory (specifically the LHV theory). In another word, the correlations can be explained by some local hidden variables, classical in nature, which are established at the source. This assumption is known as the "realism condition".

2. Measurements made by Alice and Bob are independent of each other. This assumption is known as the "locality condition".

From the above assumptions, the joint probability $P(i,j|\alpha,\beta,\lambda)$ of Alice and Bob obtaining the measurement result i and j with analyzer setting α and β, respectively with certain dependence on the local hidden variable λ, can be expressed as the product of the individual measurement probability

$$P(i,j|\alpha,\beta,\lambda) = P(i|\alpha,\lambda)P(j|\beta,\lambda). \tag{5.7}$$

Using Eq. 5.7, a correlation function $E^{LHV}(\alpha,\beta)$ taking into account any LHVs can be defined as

$$E^{LHV}(\alpha,\beta) = \int d\lambda f(\lambda)\overline{A}(\alpha,\lambda)\overline{B}(\beta,\lambda), \tag{5.8}$$

where $\overline{A}(\alpha,\lambda)$ and $\overline{B}(\beta,\lambda)$ are the average value of the measurement outcomes obtained by Alice and Bob with analyzer setting α and β, respectively. The function $f(\lambda)$ is a probability density function that is dependent on the hidden variable λ.

A Stern-Gerlach type spin measurement on a spin-1 particle will yield three possible outcomes; $-\hbar$, 0, and $+\hbar$. These can be written as the basis states $|-1\rangle$, $|0\rangle$, and $|+1\rangle$, respectively in the quantum state vector notation. If we assign the value of $+1$ to the measurement result $|-1\rangle$ and $|+1\rangle$ and the value of -1 to the measurement result $|0\rangle$,

the average values of the measurement outcomes obtained by Alice and Bob with their respective analyzer setting α and β can be written as

$$\overline{A}(\alpha,\lambda) = P(1|\alpha,\lambda) - P(0|\alpha,\lambda) + P(-1|\alpha,\lambda), \tag{5.9}$$

$$\overline{B}(\beta,\lambda) = P(1|\beta,\lambda) - P(0|\beta,\lambda) + P(-1|\beta,\lambda). \tag{5.10}$$

This will imply that $|\overline{A}(\alpha,\lambda)| \leq 1$ and $|\overline{B}(\alpha,\lambda)| \leq 1$. It is worth noting that this specific choice of $\overline{A}$ and $\overline{B}$ is not optimal for spin-1 states, i.e. the violation achieved with this specific choice of $\overline{A}$ and $\overline{B}$ is not the maximum obtainable with any general spin-1 Bell inequality. There have been numerous theoretical studies [13, 71, 106] on the optimization of the choice of $\overline{A}$ and $\overline{B}$ in this regard. However, these theoretical proposals often require more complicated measurements to be carried out for the violation of the Bell inequalities.

The difference and sum between the correlation function $E^{LHV}(\alpha,\beta)$ for different analyzer setting α and β are given by

$$E^{LHV}(\alpha,\beta) - E^{LHV}(\alpha,\beta') = \int d\lambda f(\lambda)\overline{A}(\alpha,\lambda)[\overline{B}(\beta,\lambda) - \overline{B}(\beta',\lambda)], \tag{5.11}$$

$$E^{LHV}(\alpha',\beta) + E^{LHV}(\alpha',\beta') = \int d\lambda f(\lambda)\overline{A}(\alpha',\lambda)[\overline{B}(\beta,\lambda) + \overline{B}(\beta',\lambda)]. \tag{5.12}$$

Given that $|\overline{A}(\alpha,\lambda)| \leq 1$, it is possible to rewrite Eq. 5.11 and Eq. 5.12 into the following inequalities

$$|E^{LHV}(\alpha,\beta) - E^{LHV}(\alpha,\beta')| \leq \int d\lambda f(\lambda)|\overline{B}(\beta,\lambda) - \overline{B}(\beta',\lambda)|, \tag{5.13}$$

$$|E^{LHV}(\alpha',\beta) + E^{LHV}(\alpha',\beta')| \leq \int d\lambda f(\lambda)|\overline{B}(\beta,\lambda) + \overline{B}(\beta',\lambda)|. \tag{5.14}$$

Since $|\overline{B}(\alpha,\lambda)| \leq 1$, using the triangle inequality relation*, we obtain

$$|\overline{B}(\beta,\lambda) - \overline{B}(\beta',\lambda) + \overline{B}(\beta,\lambda) + \overline{B}(\beta',\lambda)| \leq 2. \tag{5.15}$$

The spin-1 CHSH inequality can then be defined as

$$S \equiv |E(\alpha,\beta) - E(\alpha,\beta') + E(\alpha',\beta) + E(\alpha',\beta')| \leq 2. \tag{5.16}$$

With any system exhibiting only classical correlations, the maximum value of S obtainable is 2. The stronger correlations found within entangled quantum systems will lead

*The triangle inequality relation is defined as $|x+y| \leq |x| + |y|$, where x and y are real numbers.

to a value of $S > 2$, violating the inequality. This result is true as long as the choice $\overline{A}(\alpha, \lambda)$ and $\overline{B}(\beta, \lambda)$ is such that $|\overline{A}(\alpha, \lambda)| \leq 1$ and $|\overline{B}(\alpha, \lambda)| \leq 1$, i.e. the same CHSH inequality is obtained for the spin-$\frac{1}{2}$ case [105] with $|\overline{A}(\alpha, \lambda)| \leq 1$ and $|\overline{B}(\alpha, \lambda)| \leq 1$.

5.3 Derivation of the Maximum Violation for the Spin-1 CHSH Inequality

From quantum mechanics, the joint probability describing the measurement result of Alice and Bob can no longer be decoupled into the product of the individual measurement probability. Thus, to be consistent with predictions of quantum mechanics, the correlation function $E^{QM}(\alpha, \beta)$ for a bipartite system consisting of spin-1 particles is now written as

$$\begin{aligned} E^{QM}(\alpha,\beta) &= P(1,1|\alpha,\beta) - P(1,0|\alpha,\beta) + P(1,-1|\alpha,\beta) \\ &- P(0,1|\alpha,\beta) + P(0,0|\alpha,\beta) - P(-1,1|\alpha,\beta) \\ &+ P(-1,1|\alpha,\beta) - P(-1,0|\alpha,\beta) + P(-1,-1|\alpha,\beta), \end{aligned} \tag{5.17}$$

where $P(i, j|, \alpha, \beta)$ is the joint probability of Alice and Bob obtaining the measurement result i and j with analyzer setting α and β, respectively.

For this derivation, we will consider the maximally entangled state $|\Phi^-\rangle^{(2)}$ in Eq. 5.6. The analytical expressions for joint probabilities* in the correlation function $E^{QM}(\alpha, \beta)$ are given by

$$\begin{aligned} P(1,1|\alpha,\beta) &= \frac{1}{3}\cos^4(\alpha+\beta), \\ P(1,0|\alpha,\beta) &= \frac{1}{6}\sin^2[2(\alpha+\beta)], \\ P(1,-1|\alpha,\beta) &= \frac{1}{3}\sin^4(\alpha+\beta), \\ P(0,1|\alpha,\beta) &= \frac{1}{6}\sin^2[2(\alpha+\beta)], \\ P(0,0|\alpha,\beta) &= \frac{1}{3}\cos^2[2(\alpha+\beta)], \\ P(0,-1|\alpha,\beta) &= \frac{1}{6}\sin^2[2(\alpha+\beta)], \\ P(-1,1|\alpha,\beta) &= \frac{1}{3}\sin^4(\alpha+\beta), \end{aligned}$$

*Refer to Section 2.3.1 for details on the derivation of analytical expressions for joint probabilities.

$$\begin{aligned} P(-1,0|\alpha,\beta) &= \frac{1}{6}\sin^2[2(\alpha+\beta)], \\ P(-1,-1|\alpha,\beta) &= \frac{1}{3}\cos^4(\alpha+\beta). \end{aligned} \tag{5.18}$$

These joint probabilities are substituted into Eq. 5.17 and after simplification, the correlation function $E^{QM}(\alpha,\beta)$ is given by

$$E^{QM}(\alpha,\beta) = \frac{1}{3}\{1+2\cos[4(\alpha+\beta)]\}. \tag{5.19}$$

By substituting Eq. 5.19 into Eq. 5.16, an analytical expression for S for the maximally entangled state $|\Phi^-\rangle^{(2)}$ can be obtained. Maximization* of the value S with variables α, α', β, and β' produced a maximum theoretical value of $\mathrm{S} \approx 2.552$ at $\alpha(\alpha') = 56.9\,^\circ(79.4\,^\circ)$ and $\beta(\beta') = 21.9\,^\circ(89.4\,^\circ)$.

To provide a more intuitive insight into how the choice of analyzer setting β and β' lead to maximum violation given the setting of α and α' on the other analyzer, we plotted the correlation function $E(\alpha,\beta)$ for $\alpha(\alpha') = 56.9°(79.4°)$ over a range of angle β and β' in Fig. 5.3. From Eq. 5.16 it is possible to see that the maximum value of S occurs when the both the term $E(\alpha,\beta) + E(\alpha',\beta)$ and $E(\alpha',\beta) - E(\alpha,\beta')$ are maximal. The first term $E(\alpha,\beta) + E(\alpha',\beta)$ is maximal at the larger of the two intersections between the two plots in Fig. 5.3, while the maximum of the second term $E(\alpha',\beta') - E(\alpha,\beta')$ can be found at the center of two adjacent intersections between the two plots. These two angles correspond to the earlier obtained analyzer settings $\beta(\beta') = 21.9\,^\circ(89.4\,^\circ)$ which give maximal violation. This observation can be used to easily determine the maximum of S, given any two correlation functions $E(\alpha,\beta)$ and $E(\alpha',\beta)$.

The maximally entangled state $|\Phi^-\rangle^{(2)}$ in Eq. 5.6 is an idealized model describing the polarization state of the entangled photons from the source. A more realistic model will need to take into account some form of noise contribution within the system. Since our setup uses pump pulses of much shorter duration than the coincidence time window, we can assume the noise term will consist of contribution only from the individual terms in the pure state $|\Phi^-\rangle^{(2)}$ itself. Such a noise contribution, called colored noise, can be written as

$$\rho_{noise} = \frac{1}{3}(|1\rangle_1|1\rangle_2\langle 1|_1\langle 1|_2 + |0\rangle_1|0\rangle_2\langle 0|_1\langle 0|_2 + |-1\rangle_1|-1\rangle_2\langle -1|_1\langle -1|_2). \tag{5.20}$$

*The maximization of the value of S with variables α, α', β, and β' is carried out in Mathematica using the "NMaximize" function.

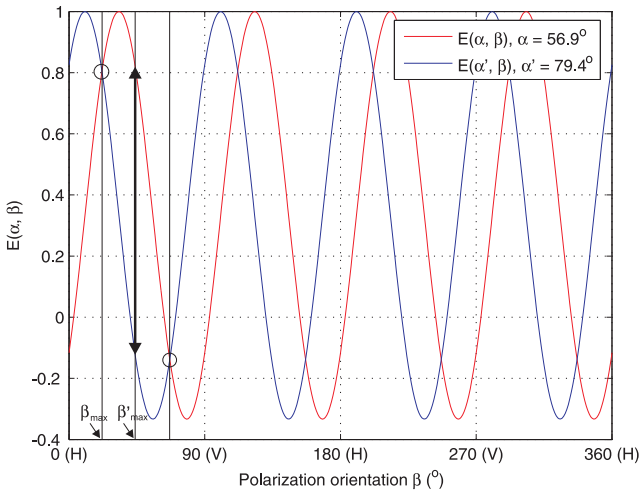

Figure 5.3: Theoretical correlation function E(α, β) and E(α', β) with $\alpha(\alpha') = 56.9\,°(79.4\,°)$ over a range of β and β' corresponding to the maximally entangled state $|\Phi\rangle$. From Eq. 5.16 it can be seen that the maximum of S occurs when the both the term $E(\alpha, \beta) + E(\alpha', \beta)$ and $E(\alpha', \beta') - E(\alpha, \beta')$ are maximal. The first term $E(\alpha, \beta) + E(\alpha', \beta)$ is maximal at the larger of the two intersections (circles) between the two plots, while the maximum of the second term $E(\alpha', \beta') - E(\alpha, \beta')$ (double arrow) can be found at the center of two adjacent intersections between the two plots. These two angles correspond to the analyzer settings $\beta(\beta') = 21.9\,°(89.4\,°)$.

In this particular situation, we are considering the special case where the individual terms in the colored noise contribution are equal, though this may not always be true in general. With the noise, the system can now only be described by a density matrix ρ consisting of a contribution from the pure state $|\Phi^-\rangle^{(2)}$ and a colored noise contribution ρ_{noise} given by

$$\rho \;=\; p|\Phi^-\rangle^{(2)}\langle\Phi^-|^{(2)} \;+\; (1-p)\rho_{noise}. \tag{5.21}$$

The relative weight between the contribution from the pure state $|\Phi^-\rangle^{(2)}$ and from the colored noise is described by the parameter p. With the colored noise contribution, the correlation function $E(\alpha,\beta,p)$ is now given by

$$\begin{aligned} E(\alpha,\beta,p) \;&=\; \frac{1}{6}\{1+p-(1-p)\cos(4\beta)+\cos(4\alpha)[1 \\ &-\; p+(3+p)\cos(4\beta)] - 4p\sin(4\alpha)\sin(4\beta)\}. \end{aligned} \tag{5.22}$$

By substituting Eq. 5.22 into Eq. 5.16, it is possible to evaluate the maximum of S for various values of p (Fig. 5.4). It can be seen that the maximally entangled state $|\Phi^-\rangle^{(2)}$ is highly resistant to colored noise. The state $|\Phi^-\rangle^{(2)}$ only fails to violate the CHSH inequality in the limit of complete colored noise contribution.

5.4 Experimental Violation of the Spin-1 CHSH Inequality

With the presence of noise in the system, the settings $\alpha(\alpha') = 56.9\,^\circ(79.4\,^\circ)$ and $\beta(\beta') = 21.9\,^\circ(89.4\,^\circ)$ derived for a pure the maximally entangled state $|\Phi^-\rangle^{(2)}$ will not yield the maximum violation. Thus, for the experimental violation of the spin-1 CHSH inequality, the analyzer setting $\alpha(\alpha') = 56.9\,^\circ(79.4\,^\circ)$ are fixed and the nine possible combinations of four-fold coincidence shown in Eq. 5.18 are recorded over a range of β and β'. Each of the joint probability terms in the correlation function $E(\alpha,\beta)$ is then evaluated by*

$$P(i,j|\alpha,\beta) = \frac{n_{ij}(\alpha,\beta)}{\sum\limits_{i,j} n_{ij}(\alpha,\beta)}, \tag{5.23}$$

where $n_{ij}(\alpha,\beta)$ is the number of four-fold coincidences obtained with measurement outcome i and j when the analyzer setting is α and β, respectively. The maximum of

*This evaluation assumes "fair sampling" which states the sample of detected pairs is representative of the pairs emitted, independent of the detection efficiency.

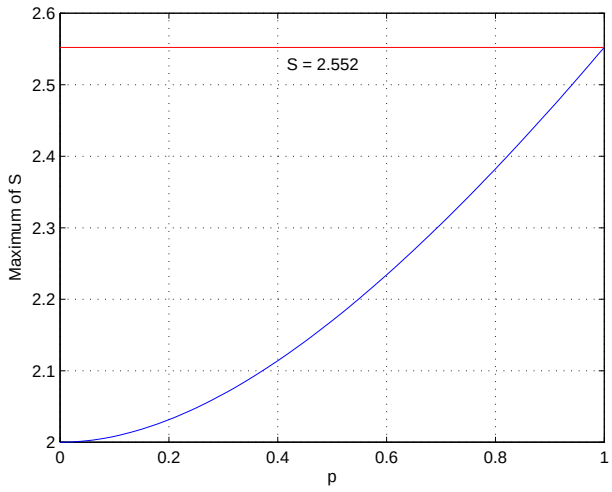

Figure 5.4: The maximum of S evaluated with various relative weight p between the contribution from the pure state $|\Phi^-\rangle^{(2)}$ and from the colored noise. It can be seen that the maximally entangled state $|\Phi^-\rangle^{(2)}$ is highly resistant to colored noise. The state $|\Phi^-\rangle^{(2)}$ only fails to violate the CHSH inequality in the limit of complete colored noise contribution.

S can then be obtained with the method suggested in the previous section. Deduction of the corresponding standard error of the maximum of S is made by propagating the Poissonian counting statistics of the four-fold coincidence events [77].

The correlation function with $\alpha(\alpha') = 56.9\,^\circ(79.4\,^\circ)$ taken without any spectral filtering is shown in Fig. 5.5 (upper panel). From the two measured correlation functions, we obtained a maximal value of $S = 2.18 \pm 0.02$ at $\beta(\beta') = 63.4^\circ(85.5^\circ)$, violating the spin-1 CHSH inequality by 9 standard deviations. From the fit of the two measured correlation functions to Eq. 5.22 with $\alpha(\alpha') = 56.9\,^\circ(79.4\,^\circ)$, we obtain $p \approx 0.78$.

The same measurements are repeated for the case with spectral filtering in the form of interference filters with a 5 nm bandwidth (FWHM) placed in the optical path before the polarization analyzers. The measured correlation functions are shown in Fig. 5.5 (lower panel). With the application of spectral filtering, the maximum of S increase to $S = 2.49 \pm 0.06$ at $\beta(\beta') = 64.4^\circ(84.9^\circ)$, more than 8 standard deviations away from the classical limit of $S = 2$. From the fit of the two measured correlation function to Eq. 5.22, we obtain a higher contribution of the pure state $|\Phi^-\rangle^{(2)}$ with $p \approx 0.85$.

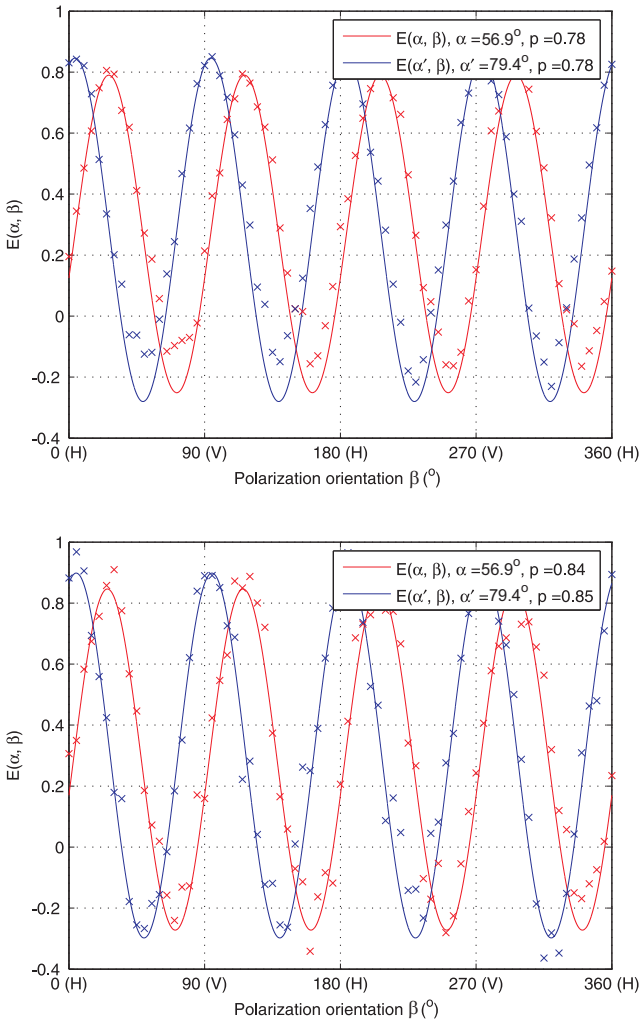

Figure 5.5: Measured correlation function E(α, β) with $\alpha(\alpha') = 56.9\,^\circ(79.4\,^\circ)$ (crossed traces). For the case with no spectral filtering (upper panel), we obtained a maximal value of $S = 2.18 \pm 0.02$ at $\beta(\beta') = 63.4^\circ(85.5^\circ)$. For the case with spectral filtering using interference filters with a 5 nm bandwidth (FWHM) placed in the optical path before the polarization analyzers (lower panel), we obtained a maximal value of $S = 2.49 \pm 0.06$ at $\beta(\beta') = 64.4^\circ(84.9^\circ)$. From a fit of the measured correlation function to Eq. 5.22 with $\alpha(\alpha') = 56.9\,^\circ(79.4\,^\circ)$ (solid traces), we obtain $p \approx 0.78$ and $p \approx 0.85$ for the case without and with spectral filtering, respectively.

From the previous experiment, we have shown that the spectral compensation scheme have fully eliminated the spectral distinguishability between the down-converted components. Thus, this increase in the proportion of the pure state $|\Phi^-\rangle^{(2)}$ cannot be attributed to the reduction of spectral distinguishability when spectral filtering is applied. One possible explanation for this phenomenon is that not all the double pairs produced in the second-order down-conversion process are coherent with each other. Instead of the maximally entangled four-photon state given in Eq. 5.5, these incoherent pairs are described by the product of two $|\Phi^-\rangle$ state in Eq 5.4.

This is possibly due the fact that the coherence length of the pump pulses in the setup is shorter than the length of the down-conversion crystal. Thus, there is a finite probability of down-conversion processes occurring at sites in the crystal separated by a a distance greater than the coherence length of the down-converted photons. Through spectral filtering, we are actually reducing their bandwidth and while increasing the coherence length. This results in better overlap between the temporal envelope of the down-converted photons giving, rise to a larger proportion of coherent pairs.

Chapter 6

Final Remarks

As we have seen in Chapter 1, a lot of the benefits offered by performing information processing and communication in the quantum regime only comes in when dealing with systems consisting of a large number of particles. To fully exploit these benefits, we are seeing an increasing number of quantum algorithms and communication protocols involving the use of quantum systems with more than two particles being proposed [16, 17, 47, 56]. Following suit, experimental implementations that allow us to generate, study, and manipulate these multi-particle systems are fast becoming commonplace [14, 57, 62, 74, 77, 107].

These implementations often involved the use of polarization-entangled photons as carriers of quantum information. One way of generating these polarization-entangled multi-photon states is through the spontaneous parametric down-conversion (SPDC) of ultrafast optical pump pulses [14, 77, 107]. Our ultimate goal here is the implementation of a high quality polarization-entangled multi-photon source based on the same SPDC. This source can be used in various quantum communication protocols and fundamental tests of quantum physics in higher-dimensional Hilbert spaces.

A major drawback often associated with these pulsed SPDC configurations is a degraded quality of polarization entanglement. This problem can only be mitigated to a certain extent through the spectral filtering of the down-converted photons. To understand this phenomenon, we implemented a photon pair source using traditional type-II phase matching in a crossed-ring configuration [7], followed by polarization analyzers and grating monochromators to resolve the different spectral components for

both photons.

In Chapter 3, I reported on a spectrally resolved polarization correlation experiments with photons produced by SPDC in a femtosecond pump regime. The objective there was to clarify the relation between entanglement quality and spectral distinguishability of the decay paths contributing to the entangled state. Through the joint spectral mapping of the polarization, we found that the two decay paths are distinguishable in their spectral properties. Leakage of polarization information into degrees of freedom which are not normally monitored results in mixedness of the polarization state of the photon pair and in turn a degradation in polarization entanglement. All our experimental results can be explained by a simple model in which the polarization states are pure, though not maximally entangled for every wavelength pair. In this model, no additional degrees of freedom are necessary to usefully describe the detected states.

Using the spectrally resolved polarization correlations we constructed a map of the entanglement entropy over the joint spectrum of the down-converted pairs, showing that the entanglement is maximal at those positions which have equal contributions from the two decay paths. The presented virtual filtering technique could be useful in finding the optimal choice of filters given a particular entanglement figure-of-merit to be maximized in combination with a count rate [97].

In Chapter 4, we conducted an experimental study on the spectral compensation scheme proposed and first implemented by Kim *et al.* in [1]. We showed that the compensation scheme eliminated the spectral distinguishability between the two decay paths. This is demonstrated by the identical joint spectra measured in the natural basis of the down-conversion, and direct correlation measurements at different power levels. The balanced contribution between the two down-conversion paths for all spectral components does not reveal any information about the polarization state, thus entanglement quality is preserved when the spectral degree of freedom is ignored. After taking the higher-order contributions into consideration, we achieved a high visibility of $V_{45} = 97.9 \pm 0.5\%$ in the complementary basis without the need of spectral filtering. The simplicity and effectiveness of this scheme make it a useful addition to the toolkit of techniques used for efficiently preparing entangled states of two and more photons.

In Chapter 5, using the source of polarization-entangled photons implemented in the previous experiment, we violated the spin-1 CHSH inequality [34]. The standard

error of the S can be obtained by propagating the Poissonian counting statistics of the four-fold coincidence events [77]. For the case when no spectral filtering is applied to the down-converted photons, we obtained a value of $S = 2.18 \pm 0.02$, violating the spin-1 CHSH inequality by 9 standard deviations. Fit of the measured correlation functions to a model that takes into account of colored noise contribution revealed we only have approximately 78 % contribution from the maximally entangled state $|\Phi\rangle$ (Eq. 5.6) in our source. With the application of spectral filtering, the maximum value of S obtained increased to $S = 2.49 \pm 0.06$, more than 8 standard deviations away from the classical limit of $S = 2$. A similar fit of the measured correlation functions yielded a higher contribution of approximately 85 % from the maximally entangled state $|\Phi\rangle$ [108].

One possible explanation can be offered for this increase in the proportion of the maximally entangled state $|\Phi\rangle$ with spectral filtering: not all the double pairs produced in the second-order down-conversion process are coherent with each other. This is possibly due the fact that the coherence length of the pump pulses in the setup are shorter than the length of the down-conversion crystal. Thus there is a finite probability of down-conversion processes occurring at different sites in the crystal separated by a distance greater than the coherence length of the down-converted photons. Through spectral filtering, we are reducing the bandwidth of the down-converted photons while increasing their coherence length. This results in a better overlap between the temporal envelope of the down-converted photons giving rise to a larger proportion of coherent double pairs. The presented spectral compensation scheme would not remove this problem.

The question that now remains is whether we have achieved the goal of implementing a high quality polarization-entangled multi-photon source. In a limited sense the answer is yes. As we have seen in Chapter 4 the problem of spectral distinguishability has been eliminated. The remaining problem of incoherent double pair production can be easily overcome by either increasing the temporal width of the pump pulses or utilizing a shorter crystal. This ensures that we are operating in a regime where the coherence length of the pump pulses are longer than the crystal thickness. However, both of these measures are likely to detrimentally impact the rate of multi-photon events. A more preferable measure that does not drastically reduce the multi-photon coincidence rate is the implementation of a temporal compensation scheme involving a double-pass configuration of the pump beam [14, 92]. This compensation scheme restores

the temporal indistinguishability between the various combinations in the maximally entangled state $|\Phi^-\rangle^{(2)}$ and is the subject of ongoing research.

Bibliography

[1] Y.-H. Kim and W. P. Grice. Generation of pulsed polarization-entangled two-photon state via temporal and spectral engineering. *Journal of Modern Optics*, **49**:2309–2323, 2002. v, 16, 39, 52, 57, 83

[2] A. Aspect, P. Grangier, and G. Roger. Experimental Tests of Realistic Local Theories via Bell's Theorem. *Physical Review Letters*, **47**:460–463, 1981. vii, 2, 9, 10, 17, 39

[3] C. A. Kocher and E. D. Commins. Polarization Correlation of Photons Emitted in an Atomic Cascade. *Physical Review Letters*, **18**:575–577, 1967. vii, 17, 18

[4] D. C. Burnham and D. L. Weinberg. Observation of Simultaneity in Parametric Production of Optical Photon Pairs. *Physical Review Letters*, **25**:84–87, 1970. viii, 2, 18, 20, 38

[5] W. P. Grice, and I. A. Walmsley. Spectral information distinguishability in type-II down-conversion with a broadband pump. *Physical Review A*, **56**:1627–1634, 1997. xii, 52, 55, 56

[6] C. H. Bennett, F. Bessette, G. Brassard, L. Salvail, and J. Smolin. Experimental quantum cryptography. *Journal of Cryptology*, **5**:3–28, 1992. 2, 11

[7] P. G. Kwiat, K. Mattle, H. Weinfurter, A. Zeilinger, A. V. Sergienko, and Y. Shih. New High-Intensity Source of Polarization-Entangled Photon Pair. *Physical Review Letters*, **75**:4337–4341, 1995. 2, 3, 9, 24, 26, 38, 39, 40, 41, 53, 57, 58, 70, 82

[8] D. Bouwmeester, J.-W. Pan, K. Mattle, M. Eibl, H. Weinfurter, and A. Zeilinger.

Experimental quantum teleportation. *Nature*, **390**:575–579, 1997. 2, 15, 19, 38, 39, 56

[9] F. A. Bovino, P. Varisco, A. M. Colla, G. Castagnoli, G. D. Giuseppe, and A. V. Sergienko. Effective fiber-coupling of entangled photons for quantum communication. *Optics Communications*, **227**:343–348, 2003. 2, 39

[10] C. Branciard, N. Brunner, N. Gisin, C. Kurtsiefer, A. Lamas-Linares, A. Ling, and V. Scarani. Testing quantum correlations versus single-particle properties within Leggett's model and beyond. *Nature Physics*, **4**:681–685, 2008. 2, 18, 38

[11] S. Gaertner, C. Kurtsiefer, M. Bourennane, and H. Weinfurter. Experimental Demonstration of Four-Party Quantum Secret Sharing. *Physical Review Letters*, **98**:020503, 2007. 2

[12] J. Suzuki, G. N. M. Tabia, and B.-G. Englert. Symmetric construction of reference-frame-free qudits. *Physical Review A*, **78**:052328, 2008. 2

[13] D. Collins, N. Gisin, N. Linden, S. Massar, and S. Popescu. Bell Inequalities for Arbitrarily High-Dimensional Systems. *Physical Review Letters*, **88**:040404, 2002. 2, 15, 30, 74

[14] J. C. Howell, A. Lamas-Linares, and D. Bouwmeester. Experimental Violation of a Spin-1 Bell Inequality Using Maximally-Entangled Four-Photon States. *Physical Review Letters*, **88**:030401, 2002. 2, 82, 84

[15] M. D. de Burgh, N. K. Langford, A. C. Doherty, and A. Gilchrist. Choice of measurement sets in qubit tomography. *Physical Review A*, **78**:052122, 2008. 2, 14, 30

[16] Proceedings 35nd Annual Symposium on Foundations of Computer Science (Shafi Goldwasser, ed.). *Algorithms for quantum computation: Discrete logarithms and factoring*. IEEE Computer Society Press, 1994. 2, 12, 82

[17] Proceedings of the twenty-eighth annual ACM symposium on Theory of computing. *A fast quantum mechanical algorithm for database search*. Association for Computing Machinery (ACM), 1996. 2, 13, 82

[18] J. Q. You and F. Nori. Superconducting Circuits and Quantum Information. *Physics Today*, **58**(11):42–47, 2005. 3

[19] C. Monroe, D. M. Meekhof, B. E. King, W. M. Itano, and D. J. Wineland. Demonstration of a Fundamental Quantum Logic Gate. *Physical Review Letters*, **75**:4714–4717, 1995. 3

[20] J. A. Jones and M. Mosca. Implementation of a quantum algorithm on a nuclear magnetic resonance quantum computer. *Journal of Chemical Physics*, **109**:1648–1653, 1998. 3

[21] F. W. Sun, Z. Y. Ou, and G. C. Guo. Projection measurement of the maximally entangled N-photon state for a demonstration of the N-photon de Broglie wavelength. *Physical Review Letters*, **73**:023808, 2006. 3

[22] J. Brendel, E. Mohler, and W. Martienssen. Experimental Test of Bell's Inequality for Energy and Time. *Europhysics Letters*, **20**:575–580, 1992. 3, 18, 38

[23] I. Marcikic, H. de Riedmatten, W. Tittel, V. Scarani, H. Zbinden, and N. Gisin. Time-bin entangled qubits for quantum communication created by femtosecond pulses. *Physical Review A*, **66**:062308, 2002. 3, 19, 23, 38, 63

[24] P. G. Kwiat, E. Waks, A. G. White, I. Appelbaum, and P. H. Eberhard. Ultrabright source of polarization-entangled photons. *Physical Review A*, **60**:R773–R776, 1999. 3, 18, 38

[25] C. Kursiefer, M. Oberparleiter, and H. Weinfurter. High-efficiency entangled photon pair collection in type-II parametric fluorescence. *Physical Review A*, **64**:023802, 2001. 3, 40, 41, 53

[26] D. Dieks. Communication by EPR devices. *Physics Letters A*, **92**:271–272, 1982. 4

[27] W. K. Wootters and W. H. Zurek. The no-cloning theorem. *Physics Today*, **62**(2):76–77, 2009. 4

[28] D. Bru, D. P. DiVincenzo, A. Ekert, C. A. Fuchs, C. Macchiavello, and J. A. Smolin. Optimal universal and state-dependent quantum cloning. *Physical Review A*, **57**:2368–2378, 1998. 4

[29] M. A. Nielsen and I. L. Chuang. *Quantum Computation and Quantum Information*. Cambridge. 5

[30] A. Einstein, B. Podolsky, and N. Rosen. Can quantum mechanical reality considered to be complete? *Physical Review*, **47**:777–780, 1935. 5

[31] J. D. Trimmer. The Present Situation in Quantum Mechanics: A Translation of Schrödinger's "Cat Paradox" Paper. *Proceedings of the American Philosophical Society*, **124**:323–338, 1980. 7

[32] D. Bohm. *Quantum Theory*. Prentice-Hall. 7, 68

[33] J. S. Bell. *Speakable and Unspeakable in Quantum Mechanics*. Cambridge University Press, 1987. 8, 15, 30, 69, 73

[34] J. F. Clauser, M. A. Horne, A. Shimony, and R. A. Holt. Proposed Experiment to Test Local Hidden-Variable Theories. *Physical Review Letters*, **23**:880–884, 1969. 8, 15, 30, 70, 73, 83

[35] J.-L. Chen, C. Wu, L. C. Kwek, and C. H. Oh. Bell inequalities for three particles. *Physical Review A*, **78**:032107, 2008. 9

[36] A. Aspect, P. Grangier, and G. Roger. Experimental Realization of Einstein-Podolsky-Rosen-Bohm *Gedankenexperiment*: A New Violation of Bell's Inequalities. *Physical Review Letters*, **49**:91–94, 1982. 9, 17, 39

[37] A. Aspect, J. Dalibard, and G. Roger. Experimental Test of Bell's Inequalities Using Time-Varying Analyzers. *Physical Review Letters*, **49**:1804–1807, 1982. 9, 17, 39

[38] Proceedings of the IEEE International Conference on Computers, Systems, and Signal Processing. *Quantum Cryptography: Public key distribution and coin tossing*, Bangalore, 1984. 11

[39] A. K. Ekert. Quantum Crytography Based on Bell's Theorem. *Physical Review Letters*, **67**:661–663, 1991. 11, 69

[40] K. Inoue, E. Waks and Y. Yamamoto. Differential Phase Shift Quantum Key Distribution. *Physical Review Letters*, **89**:037902, 2002. 11

[41] V. Scarani, A. Acín, G. Ribordy, and N. Gisin. Quantum Cryptography Protocols Robust against Photon Number Splitting Attacks for Weak Laser Pulse Implementations. *Physical Review Letters*, **92**:057901, 2004. 11

[42] D. Stucki, N. Brunner, N. Gisin, V. Scarani, and H. Zbinden. Fast and simple one-way quantum key distribution. *Applied Physics Letters*, **87**:194108, 2005. 11

[43] Y.-S. Kim, Y.-C. Jeong, and Y.-H. Kim. Implementation of polarization-coded free-space BB84 quantum key distribution. *Laser Physics*, **18**:810–814, 2008. 11

[44] A. Acín, N. Brunner, N. Gisin, S. Massar, S. Pironio, and V. Scarani. Device-Independent Security of Quantum Cryptography against Collective Attacks. *Physical Review Letters*, **98**:230501, 2007. 12

[45] A. Ling, M. P. Peloso, I. Marcikic, V. Scarani, A. Lamas-Linares, and C. Kurtsiefer. Experimental quantum key distribution based on a Bell test. *Physical Review A*, **78**:020301, 2008. 12

[46] Proceedings of the Royal Society of London A. *Quantum Theory, the Church-Turing Principle and the Universal Quantum Computer*. 12

[47] Proceedings of the Royal Society of London A. *Rapid solutions of problems by quantum computation*. 12, 82

[48] R. L. Rivest, A. Shamir, and L. Adleman. A Method for Obtaining Digital Signatures and Public-Key Cryptosystems. *Communications of the ACM*, **21**(2):120–126, 1978. 12

[49] M. Fox. *Quantum Optics: An Introduction*. Oxford University Press. 13, 21

[50] C.-Y. Lu, D. E. Browne, T. Yang, and J.-W. Pan. Demonstration of a Compiled Version of Shor's Quantum Factoring Algorithm Using Photonic Qubits. *Physical Review Letters*, **99**:250504, 2007. 13

[51] B. P. Lanyon, T. J. Weinhold, N. K. Langford, M. Barbieri, D. F. V. James, A. Gilchrist, and A. G. White. Experimental Demonstration of a Compiled Version of Shor's Algorithm with Quantum Entanglement. *Physical Review Letters*, **99**:250505, 2007. 13

[52] M. Feng. Grover search with pairs of trapped ions. *Physical Review A*, **63**:052308, 2001. 13

[53] R. Das, T. S. Mahesh, and A. Kumar. Experimental implementation of Grovers search algorithm using efficient quantum state tomography. *Chemical Physics Letters*, **369**:8–15, 2003. 13

[54] D. Gottesman. Theory of fault-tolerant quantum computation. *Physical Review A*, **57**:127–137, 1998. 14

[55] A. M. Steane. Efficient fault-tolerant quantum computing. *Nature*, **399**:124–126, 1999. 14

[56] D. Gottesman and I. L. Chuang. Demonstrating the viability of universal quantum computation using teleportation and single-qubit operations. *Nature*, **402**:390–393, 1999. 14, 82

[57] N. Kiesel, C. Schmid, U. Weber, G. Tóth, O. Gühne, R. Ursin, and H. Weinfurter. Experimental Analysis of a Four-Qubit Photon Cluster State. *Physical Review Letters*, **95**:210502, 2005. 14, 82

[58] Q. Zhang, A. Goebel, C. Wagenknecht, Y.-A. Chen, B. Zhao, T. Yang, A. Mair, J. Schmiedmayer, and J.-W. Pan. Experimental quantum teleportation of a two-qubit composite system. *Nature Physics*, **2**:678–682, 2006. 14

[59] A. M. Goebel, C. Wagenknecht, Q. Zhang, Y.-A. Chen, and J.-W. Pan. Teleportation-Based Controlled-NOT Gate for Fault-Tolerant Quantum Computation. *arXiv:0809.3583*, 2008. 14

[60] J.-W. Pan, D. Bouwmeester, H. Weinfurter, and A. Zeilinger. Experimental Entanglement Swapping: Entangling Photons That Never Interacted. *Physical Review Letters*, **80**:3891–3894, 1998. 14, 39, 69

[61] X.-B. Wang, B. S. Shi, A. Tomita, and K. Matsumoto. Quantum entanglement swapping with spontaneous parametric down-conversion. *Physical Review A*, **69**:014303, 2004. 14, 69

[62] A. M. Goebel, C. Wagenknecht, Q. Zhang, Y.-A. Chen, K. Chen, J. Schmiedmayer, and J.-W. Pan. Multistage Entanglement Swapping. *Physical Review Letters*, **101**:080403, 2008. 14, 19, 38, 39, 56, 69, 82

[63] C. Schmid, N. Kiesel, U. K. Weber, R. Ursin, A. Zeilinger, and H. Weinfurter. Quantum teleportation and entanglement swapping with linear optics logic gates. *New Journal of Physics*, **11**:033008, 2009. 14, 69

[64] M. Żukowski, A. Zeilinger, and H. Weinfurter. Entangling Photons Radiated by Independent Pulsed Sources. *Annals of the New York Academy of Sciences*, **755**:91–102, 1995. 14, 19, 38, 56

[65] D. F. V. James, P. G. Kwiat, W. J. Munro, and A. G. White. Measurement of qubits. *Physical Review A*, **64**:052312, 2001. 14, 30

[66] J. Řeháček, B.-G. Englert, and D. Kaszlikowski. Minimal qubit tomography. *Physical Review A*, **70**:052321, 2004. 14, 30

[67] A. Ling, K. P. Soh, A. Lamas-Linares, and C. Kurtsiefer. An optimal photon counting polarimeter. *Journal of Modern Optics*, **53**:15231528, 2006. 14

[68] A. Ling, K. P. Soh, A. Lamas-Linares, and C. Kurtsiefer. Experimental polarization state tomography using optimal polarimeters. *Physical Review A*, **74**:022309, 2006. 14

[69] Y. C. Liang, D. Kaszlikowski, B.-G. Englert, L. C. Kwek, and C. H. Oh. Tomographic quantum cryptography. *Physical Review A*, **68**:022324, 2003. 15

[70] J. M. Renes. Spherical-code key-distribution protocols for qubits. *Physical Review A*, **70**:052314, 2004. 15

[71] D. Kaszlikowski, L. C. Kwek, J.-L. Chen, M. Żukowski, and C. H. Oh. Clauser-Horne inequality for three-state systems. *Physical Review A*, **65**:032118, 2002. 15, 74

[72] D. Kaszlikowski, D. K. L. Oi, M. Christandl, K. Chang, A. Ekert, L. C. Kwek, and C. H. Oh. Quantum cryptography based on qutrit Bell inequalities. *Physical Review A*, **67**:012310, 2003. 15

[73] L.-B. Fu. General Correlation Functions of the Clauser-Horne-Shimony-Holt Inequality for Arbitrarily High-Dimensional Systems. *Physical Review Letters*, **92**:130404, 2004. 15

[74] A. Lamas-Linares, J. C. Howell, C. Simon, and D. Bouwmeester. Experimental Quantum Cloning of Single Photons. *Science*, **296**:712–714, 2002. 15, 19, 38, 56, 82

[75] T. Jennewein, C. Simon, G. Weihs, H. Weinfurter, and A. Zeilinger. Quantum Cryptography with Entangled Photons. *Physical Review A*, **84**:4729–4732, 2000. 18, 38

[76] S. Gröblacher, T. Paterek, R. Kaltenbaek, Č. Brukner, M. Żukowski, M. Aspelmeyer, and A. Zeilinger. An experimental test of non-local realism. *Nature*, **446**:871–875, 2007. 18, 38

[77] S. Gaertner, M. Bourennane, M. Eibl, C. Kurtsiefer, and H. Weinfurter. High-fidelity source of four-photon entanglement. *Applied Physics B*, **77**:803–807, 2003. 19, 38, 56, 79, 82, 84

[78] B. E. A. Saleh and M. C. Teich. *Fundamentals of Photonics*. Wiley-Interscience. 22, 23

[79] R. W. Boyd. *Nonlinear Optics*. Academic Press, Boston. 22

[80] S. Takeuchi. Beamlike twin-photon generation by use of type II parametric down-conversion. *Optics Letters*, **26**:843–845, 2001. 24

[81] A. V. Burlakov, M. V. Chekhova, O. A. Karabutova, and S. P. Kulik. Collinear two-photon state with spectral properties of type-I and polarization properties of type-II spontaneous parametric down-conversion: Preparation and testing. *Physical Review A*, **64**:041803, 2001. 24

[82] C. Kurtsiefer, M. Oberparleiter, and H. Weinfurter. Generation of correlated photon pairs in type-II parametric down conversion-revisited. *Journal of Modern Optics*, **48**:1997–2007, 2001. 24

[83] C. H. Bennett, H. J. Bernstein, S. Popescu, and B. Schumacher. Concentrating partial entanglement by local operations. *Physical Review A*, **53**:2046–2052, 1996. 29, 52, 69

[84] B. Schumacher. Sending entanglement through noisy quantum channels. *Physical Review A*, **54**:2614–2628, 1996. 29, 69

[85] H. de Riedmatten, V. Scarani, I. Marcikic, A. Acín, W. Tittel, H. Zbinden, and N. Gisin. Two independent photon pairs versus four-photon entangled states in parametric down conversion. *Journal of Modern Optics*, **51**:1637–1649, 2004. 37

[86] D. Bouwmeester, A. Ekert, and A. Zeilinger. *The physics of quantum information*. Springer. 38

[87] D. N. Klyshko. *Photons and Nonlinear Optics*. Gordon and Breach Science Publishers, 1970. 38, 39

[88] W. P. Grice, R. Erdmann, I. A. Walmsley, and D. Branning. Spectral distinguishability in ultrafast parametric down-conversion. *Physical Review A*, **57**:R2289–R2292, 1998. 38, 56

[89] D. Branning, W. P. Grice, R. Erdmann, and I. A. Walmsley. Engineering the Indistinguishability and Entanglement of two Photons. *Physical Review Letters*, **83**:955–958, 1999. 39, 56

[90] R. Erdmann, D. Branning, W. P. Grice, and I. A. Walmsley. Restoring dispersion cancellation for entangled photons produced by ultrashort pulses. *Physical Review A*, **62**:053810, 2000. 39, 56

[91] W. P. Grice, A. B. URen, and I. A. Walmsley. Eliminating frequency and space-time correlations in multiphoton states. *Physical Review A*, **64**:063815, 2001. 39, 56

[92] J. F. Hodelin, G. Khoury, and D. Bouwmeester. Optimal generation of pulsed entangled photon pairs. *Physical Review A*, **74**:013802, 2006. 39, 56, 84

[93] Y.-H. Kim and W. P. Grice. Measurement of the spectral properties of the two-photon state generated via type-II spontaneous parametric downconversion. *Optics Letters*, **30**:908–910, 2005. 39, 47, 56

[94] W. Wasilewski, P. Wasylczyk, P. Kolenderski, K. Banaszek, and C. Radzewicz. Joint spectrum of photon pairs measured by coincidence Fourier spectroscopy. *Optics Letters*, **31**:1130–1132, 2006. 39, 56

[95] M. Avenhaus, M. V. Chekhova, L. A. Krivitsky, G. Leuchs, and C. Silberhorn. Experimental verification of high spectral entanglement for pulsed waveguided spontaneous parametric down-conversion. *Physical Review A*, **79**:043836, 2009. 39, 56

[96] A. Ling, P. Y. Han, A. Lamas-Linares, and C. Kurtsiefer. Preparation of bell states with controlled white noise. *Laser Physics*, **16**:1140–1144, 2006. 45

[97] H. S. Poh, C. Y. Lum, I. Marcikic, A. Lamas-Linares, and C. Kurtsiefer. Joint spectrum mapping of polarization entanglement in spontaneous parametric down-conversion. *Physical Review A*, **75**:043816, 2007. 47, 56, 61, 64, 83

[98] T. E. Keller and M. H. Rubin. Theory of two-photon entanglement for spontaneous parametric down-conversion driven by a narrow pump pulse. *Physical Review A*, **56**:1534–1541, 1997. 56

[99] M. Atatüre, A. V. Sergienko, B. M. Jost, B. E. A. Saleh, and M. C. Teich. Partial Distinguishability in Femtosecond Optical Spontaneous Parametric Down-Conversion. *Physical Review Letters*, **83**:1323–1326, 1999. 56

[100] T. B. Pittman, D. V. Strekalov, A. Migdall, M. H. Rubin, A. V. Sergienko, and Y. H. Shih. Can Two-Photon Interference be Considered the Interference of Two Photon. *Physical Review Letters*, **77**:1917–1920, 1996. 57

[101] Y.-H. Kim. Two-photon interference without bunching two photons. *Physics Letters A*, **315**:352–357, 2003. 57

[102] C. K. Hong, Z. Y. Ou, and L. Mandel. Measurement of Subpicosecond Time Intervals between Two Photons by Interference. *Physical Review Letters*, **59**:2044–2046, 1987. 57

[103] A. Uhlmann. The transition probability in the state space of a *-algebra. *Reports on Mathematical Physics*, **9**:273–279, 1976. 69

[104] C. A. Fuchs. *Distinguishability and Accessible Information in Quantum Theory.* PhD thesis, University of New Mexico. 69

[105] D. Heiss. *Fundamentals of Quantum Information: Quantum Computation, Communication, Decoherence and All That (Lecture Notes in Physics).* Springer. 73, 75

[106] D. Kaszlikowski, P. Gnaciński, M. Żukowski, W. Miklaszewski, and A. Zeilinger. Violations of Local Realism by Two Entangled N-Dimensional Systems Are Stronger than for Two Qubits. *Physical Review Letters*, **85**:4418–4421, 2000. 74

[107] C.-Y. Lu, X.-Q. Zhou, O. Gühne, W.-B. Gao, J. Zhang, Z.-S. Yuan, A. Goebel, T. Yang, and J.-W. Pan. Experimental entanglement of six photons in graph states. *Nature Physics*, **3**:91–95, 2007. 82

[108] H. S. Poh, J. Lim, I. Marcikic, A. Lamas-Linares, and C. Kurtsiefer. Eliminating Spectral Distinguishability in Ultrafast Spontaneous Parametric Down-conversion. *arXiv:0905.3849v1*, 2009. 84